



1 **Vertical Structure and Driving Mechanism of PM<sub>2.5</sub> and PM<sub>10</sub> Aerosols**  
2 **in Hefei Based on LiDAR Observations (2021–2023)**

3 Yan Yan<sup>1</sup>, Xueliang Deng<sup>1,2,\*</sup>, Rui Dai<sup>1</sup>, Qianqian Xu<sup>1</sup>, Qinqin Huang<sup>1</sup>, Yang Liu<sup>1</sup>, Chunxuan Wei<sup>1</sup>,  
4 Jinhua Xie<sup>1</sup>, Yanfeng Li<sup>1,3</sup>, & Yan Sun<sup>4</sup>

5  
6  
7 <sup>1</sup>Hefei Meteorological Bureau, Hefei, Anhui 230061, China

8 <sup>2</sup> Heavy Rainfall Research Center of China, Wu Han, Hubei 430205, China

9 <sup>3</sup>Hefei Jichenyun Information Technology Co., Ltd., Hefei 230041, China

10 <sup>4</sup>Anhui Public Meteorological Service Center, Hefei, Anhui 230031, China

11 *Correspondence to:* Xueliang Deng ([dengxueliang9989@aliyun.com](mailto:dengxueliang9989@aliyun.com))

12  
13 **Abstract:**

14 Aerosol pollution remains a significant environmental concern in China. However, the vertical structure and  
15 evolution of particulate matter are poorly understood due to the lack of long-term, high-resolution observations. In  
16 Hefei, the aerosols during the study period were dominated by a mixture of fine particulate matter (PM<sub>2.5</sub>) and coarse  
17 particulate matter (PM<sub>10</sub>), mainly originating from urban traffic emissions, industrial activities, and regional transport,  
18 with significant contributions from secondary inorganic aerosols and occasional dust events. To address the  
19 knowledge gap in aerosol vertical distribution during different pollution episodes, this study employed an aerosol  
20 LiDAR system with 532 nm band to investigate the vertical profile characteristics of aerosols, with a focus on  
21 comparing the stratification differences of optical properties between PM<sub>2.5</sub> and PM<sub>10</sub> pollution events over Hefei  
22 across different periods and altitudes. The seasonal and diurnal variations of aerosol profiles were investigated, and  
23 vertical structures were compared on polluted and clean days. The relationship between near-surface particulate  
24 matter concentrations and aerosol stratification was analyzed, alongside the dynamic evolution of aerosol layers  
25 during typical pollution events. Our results demonstrated that the extinction coefficient (532 nm) of PM<sub>2.5</sub>-polluted  
26 days below 0.6 km was approximately three times that of PM<sub>10</sub>-polluted days. In contrast, the depolarization ratio of  
27 PM<sub>10</sub>-polluted episodes remains consistently higher than that of PM<sub>2.5</sub>-polluted cases throughout the entire observed



28 altitude range. The differences in extinction between polluted and clean days for PM<sub>2.5</sub> were most pronounced below  
29 0.9 km and subsequently decreased as altitude increased, whereas the differences in PM<sub>10</sub> remained significant below  
30 1.2 km. For PM<sub>2.5</sub>, the strongest enhancement appeared between 7:00 and 14:00 (Beijing time, BJT). A subtle lifting  
31 with height was observed around midday. PM<sub>10</sub>-polluted days were characterized by a greater vertical extension of  
32 high aerosol extinction (reaching up to ~1.2–1.4 km) but a shorter duration of strong extinction, in contrast to PM<sub>2.5</sub>-  
33 polluted days, which exhibited a more persistent but vertically confined aerosol layer. PM<sub>10</sub> pollutant tended to  
34 accumulate within the altitude range of 0.4–1.2 km on polluted days. The vertical wind shear (VWS) was weaker on  
35 PM<sub>2.5</sub>-polluted days compared to clean days. On PM<sub>10</sub>-polluted days, the VWS in the near-surface layer (1000–900  
36 hPa) was significantly stronger than that on clean days, especially during the early morning and evening periods. The  
37 PM<sub>2.5</sub> pollution in Hefei was mostly contributed by temperature inversion and high relative humidity, while PM<sub>10</sub>  
38 pollution was driven by long-range transport of aerosol particles under the cold front system and dry conditions.  
39 These findings highlight the complex interactions between aerosol optical properties, boundary-layer dynamics, and  
40 synoptic-scale meteorology, providing new insights into the vertical processes governing air quality in eastern China.  
41 **Keywords:** Aerosol LiDAR, Vertical profile, Heavy pollution episodes, Vertical wind shear, Fine and coarse  
42 particulate matter.

## 43 1. Introduction

44 Air pollution remains one of the most pressing environmental challenges globally, with fine particulate matter  
45 and inhalable coarse particles posing serious risks to public health and atmospheric visibility ([Chen et al., 2023](#); [Deng  
46 et al., 2023](#)). Air quality is closely related to the concentration of pollutants suspended in the atmosphere ([Wang et  
47 al., 2024](#)). Solid and liquid phase pollutants, known as aerosols, not only impact air quality and visibility through  
48 multiple mechanisms but also affect the climate by altering Earth's radiation budget and water cycle processes ([Chen  
49 et al., 2016](#); [Miao et al., 2018](#)). In China, substantial improvements in air quality have been achieved in recent years  
50 through stringent emission control policies. However, severe particle pollution events still occur frequently, especially  
51 in winter haze episodes and spring dust storms across the Yangtze River Delta (YRD) region ([Han and Cao 2022](#);  
52 [Wang and Wang 2021](#)). To date, most studies have focused on surface-level air pollution data obtained from ground  
53 monitoring networks ([He et al., 2021](#); [Lee et al., 2016](#); [Siddique et al., 2024](#)). These data provide critical insights into  
54 near-surface concentrations. However, they lack information on the vertical distribution and formation mechanisms  
55 of pollutants, which is essential for understanding aerosol processes in the troposphere ([Mehta et al., 2021](#); [Mishra  
56 and Shibata 2012](#); [Wang et al., 2018](#)).

57 While extensive ground-based monitoring has provided insights into surface-level pollution, the understanding



58 of the vertical distribution and evolution of aerosols remains limited due to a lack of long-term and high-resolution  
59 vertical observations ([He et al., 2022](#); [Ou et al., 2021](#); [Shen et al., 2022](#)). The atmospheric boundary layer (ABL)  
60 plays a crucial role in regulating aerosol dynamics through physical mechanisms such as turbulence, convection, and  
61 mixing ([Gao et al., 2011](#); [Garratt 1994](#); [Tombrou et al., 2007](#)). As the interface between the surface and the free  
62 troposphere, the ABL governs the vertical exchange of energy, moisture, and pollutants. Numerous studies have  
63 demonstrated that lower ABL heights could trap pollutants near the surface, leading to elevated PM<sub>2.5</sub> levels. These  
64 lower heights are often associated with thermal inversions and stagnant synoptic conditions ([Liu et al., 2020](#); [Sun et  
65 al., 2024a](#)). Under such conditions, limited mixing suppresses the vertical dispersion of aerosols, allowing surface  
66 emissions to accumulate rapidly, particularly in urban areas with high anthropogenic activity. In contrast, strong  
67 vertical mixing and higher ABL heights enhance dispersion and dilution of pollutants, which frequently results in  
68 improved surface air quality ([Jin et al., 2021](#)). Moreover, interactions between the lower ABL and the overlying free  
69 troposphere, including vertical wind shear, subsidence, and entrainment processes, also significantly influence  
70 aerosol layering and transboundary transport ([Deng et al., 2023](#); [Li et al., 2022](#)). These interactions are significant  
71 during transition periods such as the morning boundary layer growth phase or evening collapse, which strongly affect  
72 aerosol vertical distribution ([Li et al., 2018](#)). Despite these known mechanisms, detailed observations of the vertical  
73 structure of aerosols and their relation to meteorological dynamics remain limited under varying pollution conditions  
74 and across different seasons ([Yang et al., 2025](#)). Comprehensive long-term observations are still needed to  
75 characterize how meteorology influences aerosol stratification and transformation over time.

76 Active remote sensing techniques, such as aerosol Light Detection and Ranging (LiDAR), have emerged as  
77 powerful tools to fill this observational gap ([Ansmann et al., 2013](#); [Chen et al., 2024a](#)). Unlike passive satellite-based  
78 instruments, LiDAR systems provide high-resolution vertical profiles of aerosol optical properties at fine temporal  
79 scales and under both day and night conditions, capable of capturing sub-kilometer vertical gradients and diurnal  
80 variability that are critical for understanding boundary-layer dynamics ([Wang et al., 2024](#); [Zhang et al., 2020b](#)). It  
81 enables continuous monitoring of aerosol structure, boundary layer formation, and pollutant layering in response to  
82 atmospheric dynamics ([Fan et al., 2024](#); [Fang et al., 2024](#); [Li et al., 2024](#)). Specifically, polarization-sensitive aerosol  
83 LiDAR can simultaneously retrieve extinction coefficients and depolarization ratios, which serve as indications of  
84 aerosol concentration and morphology ([Cairo et al., 2024](#); [Chen et al., 2024a](#); [Kumar et al., 2024](#)). The extinction  
85 coefficient quantifies the total attenuation of light caused by scattering and absorption by particles, and it is directly  
86 related to aerosol optical depth and visibility ([Chen et al., 2024b](#); [Sun et al., 2024b](#)). The depolarization ratio  
87 distinguishes the spherical and non-spherical particles, providing insights into aerosol types such as secondary



88 inorganic aerosols, biomass burning smoke, and desert dust. These parameters are crucial for understanding not only  
89 the optical but also the physical properties of aerosols ([Chen et al., 2024b](#); [Gebauer et al., 2024](#)). However, most  
90 previous studies using such measurements have been limited to short-term campaigns or case studies of individual  
91 pollution episodes ([Chen et al., 2022](#); [Zhong et al., 2018](#)). These attempts often lack the spatial and temporal  
92 representativeness necessary for climatological or process-level understanding, particularly in regions subject to  
93 strong seasonal and meteorological variability.

94 Long-term monitoring of air pollutants is essential for the comprehensive understanding of their temporal  
95 characteristics ([Fan et al., 2021](#); [Xiang et al., 2021](#)). Unlike ground-based air quality monitoring networks, vertically  
96 resolved data are required to evaluate the entire process of pollution events, vertical mixing, and potential long-range  
97 transport ([Wang et al., 2024](#)). Passive satellite remote sensing techniques have proven useful in bridging spatial gaps  
98 in air quality data, but are limited in their ability to resolve vertical structures with high temporal accuracy due to  
99 their coarse resolution and fixed overpass times ([Chen et al., 2023](#)). Chemical transport models (CTMs) have been  
100 widely used to simulate the spatiotemporal behavior of aerosols and their interactions with meteorology ([Wang et al.,  
101 2025](#); [Xiong et al., 2023](#)). However, their accuracy is constrained by uncertainties in emissions inventories, boundary  
102 conditions, meteorological input fields, and the representation of aerosol microphysics. In addition, model  
103 performance varies significantly by region and pollution type ([Zhan et al., 2024](#)). LiDAR technology provides high  
104 spatiotemporal resolution vertical measurements of aerosol and meteorological variables, including aerosol extinction,  
105 backscattering, and wind profiles ([Chen et al., 2023](#); [Chouza et al., 2015](#); [Zhang et al., 2020b](#)). This capability makes  
106 LiDAR particularly suitable for investigating aerosol evolution and transport within the ABL and lower troposphere.  
107 Nonetheless, long-term time series analyses based on continuous LiDAR measurements remain limited in the  
108 literature.

109 To address these limitations, we conducted multi-year observations using an aerosol LiDAR system in Hefei.  
110 The deployed LiDAR system provides real-time vertical profiles of aerosol extinction and depolarization ratios,  
111 allowing for a detailed assessment of aerosol structure under different pollution levels. We characterized the vertical  
112 and temporal evolution of aerosol properties and linked them with pollution episodes and boundary-layer processes  
113 by integrating LiDAR data with surface PM<sub>2.5</sub> and PM<sub>10</sub> concentrations, meteorological observations, and reanalysis  
114 products. Therefore, the objectives of this study were (1) to analyze the seasonal and diurnal variations of vertical  
115 profiles with aerosol extinction and depolarization data; (2) to compare the vertical structures on polluted and clean  
116 days to clarify the differences in aerosol optical properties between these two conditions; (3) to assess the relationship  
117 between aerosol layering and near-surface pollutant concentrations at different heights; and (4) to investigate the



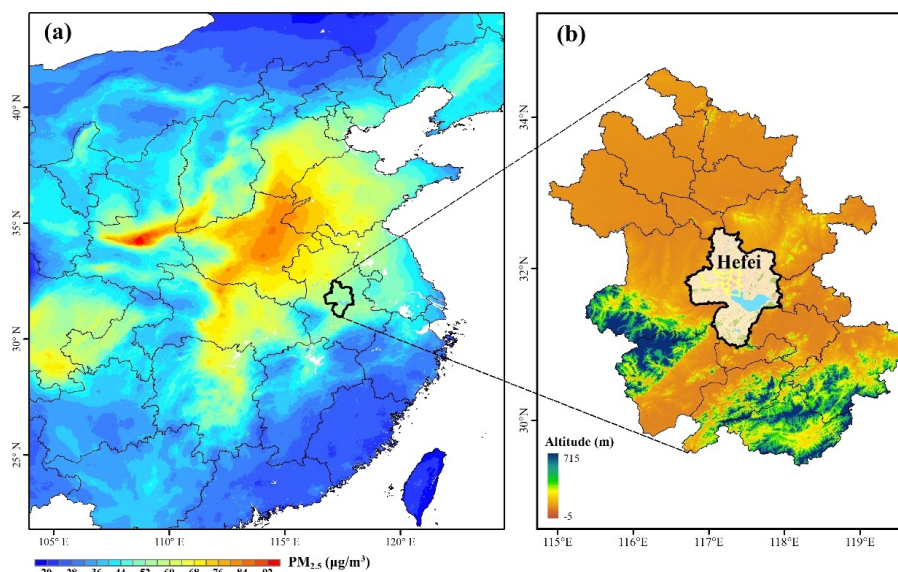
118 spatiotemporal evolution of aerosols during specific pollution episodes and explore the mechanisms of their vertical  
119 structure, meteorological conditions, and accumulation process. The findings are expected to enhance our  
120 understanding of aerosol vertical structure in eastern China and provide scientific support for air quality management  
121 and modeling efforts.

122

## 123 **2. Data and methods**

### 124 **2.1. Study region**

125 Hefei occupies a strategic location, bridging the Beijing-Tianjin-Hebei metropolitan cluster and the Yangtze  
126 River Delta economic hub. The study area lies in a transitional climatic zone, where temperature inversions occur  
127 frequently in winter. Such conditions often result in stagnant air that limits pollutant dispersion. In addition, the  
128 geography of Hefei plays a critical role in exacerbating air quality challenges. Hefei is surrounded by the Dabie  
129 Mountains in the west and the Huangshan ranges in the south. The open plains dominate its northern and eastern  
130 frontiers (**Fig. 1b**). These natural barriers hinder the southward dispersion of airborne pollutants while trapping those  
131 transported from industrialized northern regions within the basin. The unique combination of geographic constraints  
132 and atmospheric conditions has made Hefei a focal point for studying complex pollution mechanisms. Researchers  
133 here focus particularly on the synergistic effects of regional transportation, local emissions, and meteorological  
134 drivers on particulate matter formation ([Fang et al., 2024](#); [Huang et al., 2016](#); [Liu et al., 2024](#)).



135

136 **Figure 1.** The spatial distribution of (a) the averaged  $PM_{2.5}$  concentration during winter from 2021 to 2023 (Ministry  
137 of Environmental Protection in China, <https://air.cnemc.cn:18007/>) and (b) the location of the study area (Hefei,  
138 China). The digital elevation model (DEM) data are derived from the NASA Shuttle Radar Topography Mission  
139 (SRTM) 30 m product (<https://glovis.usgs.gov/>), and the land use map of the study area is obtained from the 30 m  
140 resolution annual China Land Cover Dataset (CLCD) dataset. The monitoring station is marked by the blue dot.

141

## 142 2.2. Aerosol LiDAR data

143 The LGJ-05 aerosol LiDAR combines traditional radar technology and modern laser technology with 355 nm,  
144 532 nm, and 1064 nm as detection light sources. Measurements at 532 nm were utilized exclusively for the present  
145 study. The LiDAR emits 532 nm laser pulses into the atmosphere to capture backscattered signals, thereby obtaining  
146 key aerosol optical characteristics. During the transmission process, the laser pulse is scattered and extinguished by  
147 atmospheric aerosol particles. The intensity of backscattered light at different altitudes correlates with the scattering  
148 and extinction properties of aerosol and cloud particles at those altitudes. The backscattered light from spherical  
149 particles can maintain its polarization characteristics of the emitted pulse since the emitted laser pulse is linearly  
150 polarized. In contrast, non-spherical particles (such as dust particles and ice crystals in cirrus clouds) depolarize the  
151 backscattered light due to their irregular shapes and asymmetric interaction with linearly polarized laser pulses. The  
152 LiDAR could detect the echo signals of the parallel and vertical components in the backscattered light, enabling



153 acquisition of the vertical profile of the depolarization ratio of atmospheric aerosol particles. It could enable three-  
154 dimensional monitoring of the atmosphere in real time through active remote sensing, with the capacity to invert  
155 spatiotemporal distribution information such as aerosol extinction, depolarization, and water vapor mixing ratio in  
156 the atmosphere. The aerosol extinction coefficient reflects the attenuation capacity of aerosol particles to incident  
157 light, while the depolarization ratio indicates the non-spherical nature of aerosol and cloud particles. A higher  
158 extinction coefficient typically indicates a larger concentration of aerosol particles or stronger light-  
159 scattering/absorbing properties. However, greater depolarization values denote a higher abundance of non-spherical  
160 aerosol particles (e.g., dust, rugged industrial aerosols) or mixed-phase cloud constituents. By contrast, lower  
161 depolarization ratios indicate a dominance of spherical particles or simpler particle structures.

162 The LGJ-05 aerosol LiDAR accomplishes all these operations using a laser as the light source. The laser system  
163 generates high-energy light beams at wavelengths of 532 nm, 355 nm, and 1064 nm. The three-wavelength laser  
164 beams are emitted into the atmosphere through a broadband mirror and undergo Mie scattering with aerosols. Since  
165 the instrument is capable of receiving data below 30 km, the effective detection range of the aerosol LiDAR can  
166 cover 0.2-6 km and 0.2-15 km for daytime and nighttime, respectively. It offers a vertical spatial resolution of 7.5  
167 meters and a temporal resolution of 10 minutes. The observations were conducted at the National Meteorological  
168 Observation Station in the northwest of Hefei (117.06°N, 31.96°E) from March 2021 to May 2023.

169

### 170 **2.3. Ground-based observational data**

171 Hourly concentrations of major air pollutants ( $PM_{2.5}$  and  $PM_{10}$ ) were obtained from ground-based monitoring  
172 stations in Hefei, which are operated and maintained by the China National Environmental Monitoring Centre  
173 (CNEMC) (Liu et al., 2017). These pollutant data were obtained from professional monitoring instruments, with the  
174 LGH-01B aerosol mass concentration monitor used for  $PM_{10}$  and the LGH-01B aerosol mass concentration monitor  
175 used for  $PM_{2.5}$ , both of which apply the beta attenuation method. All instruments are calibrated regularly according  
176 to national standards, and the data undergo strict quality control procedures, including hourly, daily, and annual audits,  
177 as described in the China Environmental Monitoring Quality Assurance and Quality Control Manual. It should be  
178 noted that we focused on  $PM_{2.5}$  and  $PM_{10}$  concentrations during the winter and spring seasons. The hourly resolution  
179 of the dataset allows for capturing diurnal variations in pollutant levels, while the multi-pollutant data facilitates  
180 analysis of the differences in meteorological responses of pollutants in Hefei.

181 The observed meteorological variables were obtained from the China Meteorological Administration (CMA)  
182 (<http://data.cma.cn/en>), measured by the Vaisala PTB210 Digital Barometer for atmospheric pressure, the Vaisala



183 HMP155A Temperature and Relative Humidity Probe for air temperature (T) and relative humidity (RH), the EL15-  
184 2C Wind Direction Sensor for wind direction (WD), and the EL15-1C Wind Speed Sensor for wind speed (WS). All  
185 meteorological instruments are routinely maintained and calibrated to ensure the accuracy and reliability of  
186 observational data.

187

#### 188 **2.4. ECMWF reanalysis data**

189 This study aims to investigate the impact of the synoptic system on PM<sub>2.5</sub> and PM<sub>10</sub> pollution. The ERA5  
190 reanalysis dataset, freely accessible via the Copernicus Climate Change Services platform  
191 (<https://cds.climate.copernicus.eu/datasets>), serves as the data source. Vertical atmospheric data within the ERA5  
192 dataset are interpolated to 37 pressure levels. This interpolation yields comprehensive data ranging from the Earth's  
193 surface to the upper atmosphere. Given its high spatial and temporal resolution, the ERA5 dataset has been widely  
194 employed in extreme weather events, climate prediction, and air pollution studies ([Fan et al., 2021](#); [Zhang et al.,  
195 2020b](#)).

196 This study collected hourly geopotential height, vertical wind velocity, temperature, and humidity data. The data  
197 correspond to multi-pressure levels (500 hPa, 700 hPa, 725 hPa, 750 hPa, 775 hPa, 800 hPa, 825 hPa, 850 hPa, 875  
198 hPa, 900 hPa, 925 hPa, 950 hPa, 975 hPa, and 1000 hPa) and cover the period from 2021 to 2023. The spatial  
199 resolution of our dataset was 0.25°×0.25° (zonal and meridional) and supports a detailed and accurate exploration  
200 of the synoptic-particulate matter relationship.

201

#### 202 **2.5. Quality control**

203 To explore the potential of aerosol LiDAR observations and improve data reliability, this study extracted the  
204 extinction coefficient and depolarization ratio data at 532 nm from the LiDAR system for the period from March  
205 2021 to May 2023. In the quality control process, specific criteria were established to ensure the reliability of the  
206 retrieved parameters. Specifically, it covers three steps for outlier detection, removal of spurious points, and temporal  
207 consistency analysis. Outlier detection was conducted to eliminate all records outside the normal value range  
208 according to the parameter intervals provided by the instrument. The extinction coefficient at 532 nm was calculated  
209 using data from the parallel (P) channel, which was considered reliable only when the corresponding signal-to-noise  
210 ratio (SNR) exceeded three. The depolarization ratio was derived from the P and perpendicular (S) channels, and data  
211 were accepted only when both channels had SNRs greater than three. The P channel detects linearly polarized light  
212 in the parallel direction, while the S channel detects linearly polarized light in the perpendicular direction. Based on



213 the time series of SNR records, the individual extinction and depolarization data were cross-referenced. Temporal  
214 consistency analysis was conducted by identifying records that deviated by more than three standard deviations from  
215 the mean as outliers. To further improve data reliability, this study calculates the credibility ratio of the extinction  
216 coefficient and depolarization ratio at different altitudes. Based on the criterion of a 60% valid data availability rate,  
217 the efficient detection ranges for the 532 nm of the extinction coefficient and depolarization ratio were 0.2025~1.815  
218 km.

219

## 220 **2.6. Methodology**

### 221 **2.6.1 Definition of polluted and clean**

222 In this study, the data from 2021-2023 are gathered and categorized into four seasons: spring (Mar.-May),  
223 summer (Jun.-Aug.), autumn (Sep.-Nov.), and winter (Dec.-Feb.). Given that PM<sub>2.5</sub> pollution is most severe in winter  
224 and sand-dust events are frequent in spring, the definitions of polluted and clean days in this study primarily focus  
225 on these two seasons. Days in winter when the daily average concentration of PM<sub>2.5</sub> exceeds 75 µg/m<sup>3</sup> are defined as  
226 PM<sub>2.5</sub>-polluted days. Conversely, days in winter with a daily average PM<sub>2.5</sub> concentration below 50 µg/m<sup>3</sup> are  
227 classified as PM<sub>2.5</sub>-clean days. For PM<sub>10</sub>, spring days with daily average concentrations above 150 µg/m<sup>3</sup> are defined  
228 as polluted days, while those below 100 µg/m<sup>3</sup> are considered clean days (Ministry of Environmental Protection of  
229 the People's Republic of China, Technical Regulation on Ambient Air Quality Index, 2012). To eliminate the wet  
230 deposition effect of precipitation, all observations in this study excluded precipitation daily data.

### 231 **2.6.2 Calculation of Vertical Wind Shear**

232 The vertical wind shear (VWS) is a crucial factor in characterizing the change in wind velocity with height. It  
233 is defined based on the magnitude of the difference in the bulk wind vector between two vertical levels, normalized  
234 by the height difference. The VWS can be calculated using the following formula:

$$235 \text{VWS} = \frac{\sqrt{(u_t - u_l)^2 + (v_t - v_l)^2}}{(z_t - z_l)} \times 1000 \quad (1)$$

235

236 Where VWS is measured in units of m/s·km<sup>-1</sup>.  $u_t$  and  $u_l$  denote the zonal wind components at the upper  $z_t$  and lower  
237  $z_l$  levels, respectively, while  $v_t$  and  $v_l$  represent the corresponding meridional wind components. This calculation aids  
238 in quantifying the vertical dynamic forces that may impact the dispersion and transportation of pollutants.

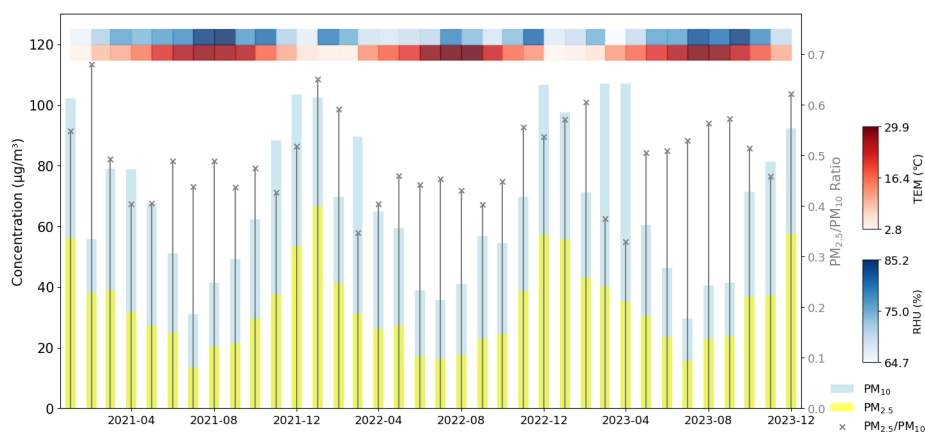
239



240 **3. Results and discussion**

241 **3.1. Variations of inter-annual PM<sub>2.5</sub> and PM<sub>10</sub>**

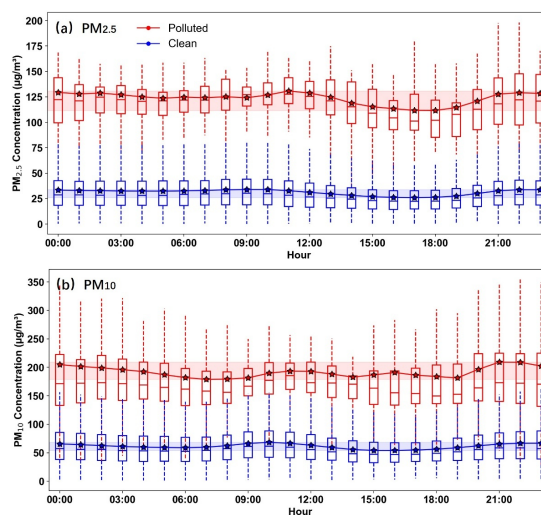
242 **Figure 2** shows the variations in the concentrations of PM<sub>2.5</sub> and PM<sub>10</sub> pollutants from 2021 to 2023. Both PM<sub>2.5</sub>  
 243 and PM<sub>10</sub> pollutants exhibited a clear seasonal pattern, with concentrations higher in winter and lower in summer  
 244 (Liu et al., 2021; Wang et al., 2024). In addition, PM<sub>10</sub> concentrations were relatively high during the spring months  
 245 of 2022 and 2023, likely driven by increased dust events such as sand-dust storms that commonly occurred during  
 246 this season. High PM<sub>2.5</sub>/PM<sub>10</sub> ratios ( $\geq 0.5$ ) during winter suggest a dominant contribution from fine particulate  
 247 matter, whereas lower ratios ( $\leq 0.5$ ) in spring indicate an increased presence of coarse particles (Liu et al., 2015).  
 248 The episodic PM<sub>10</sub> peaks observed in spring 2022–2023 coincided with a pronounced decrease in the PM<sub>2.5</sub>/PM<sub>10</sub>  
 249 ratio. This phenomenon reflected intensified pollution of coarse-mode aerosols. Although winter months also suffered  
 250 elevated PM<sub>10</sub> pollution, the concurrent high PM<sub>2.5</sub> concentrations complicated the separation of dust-related  
 251 contributions. In contrast, the lower PM<sub>2.5</sub>/PM<sub>10</sub> ratios in spring facilitated the distinct observation of dust events due  
 252 to the reduced interference from fine particulate matter.



253 **Figure 2.** Monthly variation of PM<sub>2.5</sub> (marked as the yellow bars) and PM<sub>10</sub> (marked as the blue bars)  
 254 concentrations, PM<sub>2.5</sub>/PM<sub>10</sub> ratio (the grey lines with markers on top), temperature (TEM), and relative humidity  
 255 (RH) during 2021-2023 in Hefei (Beijing time, BJT = UTC + 8 h).  
 256  
 257

258 The hourly PM<sub>2.5</sub> and PM<sub>10</sub> concentrations exhibited clear diurnal variation on both polluted and clean days (Fig.  
 259 3). Polluted days showed significantly higher PM<sub>2.5</sub> levels, with hourly averages ranging from 100 to 125 µg/m<sup>3</sup>,  
 260 compared to the stable 35–55 µg/m<sup>3</sup> range observed on clean days. The PM<sub>2.5</sub> concentrations on polluted days  
 261 displayed a bimodal pattern. The concentrations remained consistently high throughout the morning period from

262 04:00 to 11:00 (Beijing time, BJT), with the peak at 10:00–11:00 (BJT) (Dai et al., 2020). Valleys in PM<sub>2.5</sub>  
 263 concentrations occurred at 16:00 (BJT), possibly associated with enhanced atmospheric dispersion from midday  
 264 heating that facilitates the dilution of particulate matter. Concentrations initiated an upward trend from 17:00 (BJT),  
 265 with a gradual increase culminating in a peak between 21:00 and 22:00 (BJT). In contrast, clean days exhibited a  
 266 subtle morning (08:00–10:00) and overnight peaks (00:00–02:00). For PM<sub>10</sub>, polluted days presented pronounced  
 267 peaks at 10:00–12:00 and 21:00–22:00 (BJT), coinciding with increased dust resuspension or construction activities  
 268 (Yu et al., 2020). However, valleys occurred at 07:00 and 19:00 (BJT). These may be due to reduced surface  
 269 disturbances during dawn and enhanced vertical mixing in the afternoon. Clean days maintained low PM<sub>10</sub>  
 270 concentrations (50–70 µg/m<sup>3</sup>) with minor fluctuations, mirroring the PM<sub>2.5</sub> pattern. The time series curves of  
 271 pollutants had different peak times and amplitudes, indicating distinct origins. PM<sub>2.5</sub> was more influenced by  
 272 continuous anthropogenic emissions, while PM<sub>10</sub> was sensitive to episodic coarse-particle events (Deng et al., 2023;  
 273 Wang et al., 2024). These hourly dynamics highlighted the role of diurnal meteorological cycles in modulating  
 274 particulate matter distribution, with polluted days amplifying both primary emissions and secondary aerosol  
 275 formation (Liu et al., 2021).



276  
 277 **Figure 3.** Hourly mean (a) PM<sub>2.5</sub> and (b) PM<sub>10</sub> concentrations on polluted and clean days (Beijing time, BJT = UTC  
 278 + 8 h). The blue and red shaded areas represent the ranges of mean concentration values for polluted and clean days,  
 279 respectively. The whiskers and boxes represent the 95th, 75th, 50th, 25th, and 5th percentiles, respectively. The stars  
 280 represent the mean values of the pollutant concentrations. The solid lines connect the hourly mean values to show  
 281 the diurnal variation trends.



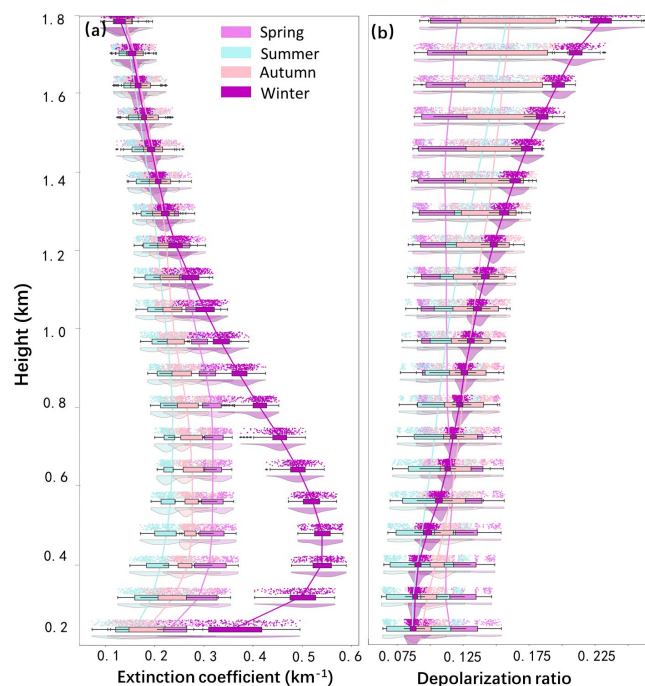
### 282 **3.2 Temporal variation of vertical distribution structure**

283 In addition to the impacts exerted by surface-level pollution, the investigation of vertical distribution is also of  
284 paramount significance for a comprehensive understanding of air quality dynamics. The extinction coefficient at 532  
285 nm shows seasonal and vertical variation. Winter presented the highest extinction values among the four seasons (**Fig.**  
286 **4a**) ([Chen et al., 2023](#); [Wang et al., 2024](#)). This was likely related to enhanced emissions from domestic heating and  
287 stagnant meteorological conditions that restrict vertical mixing ([Zhong et al., 2018](#)). In contrast, summer exhibited  
288 the lowest extinction coefficients at 532 nm across the profile, suggesting the effective dispersion of aerosols due to  
289 strong convection and a high planetary boundary layer ([Li et al., 2015](#)). Spring and autumn showed intermediate  
290 levels. Vertically, extinction coefficients were highest near the surface and gradually decreased with altitude in all  
291 seasons. The most significant differences between seasons appeared below 1 km, especially in the 0.2–0.6 km range  
292 ([Zhong et al., 2018](#)). Above 1.0 km, the extinction values in all seasons converged toward high altitude, indicating a  
293 reduced aerosol presence in the upper layer ([Liu et al., 2024](#)).

294 The depolarization ratio also exhibited seasonal differences (**Fig. 4b**). In the lower layer below 0.6 km, spring  
295 showed the highest depolarization ratios, which were attributed to a greater proportion of non-spherical particles such  
296 as mineral dust or internally mixed soot. ([Biuki et al., 2022](#)). This may result from springtime dust resuspension and  
297 aged industrial emissions. In contrast, summer had the lowest depolarization ratios, implying that aerosols were  
298 dominated by more spherical particles, such as those formed through secondary processes (e.g., sulfate or organic  
299 aerosols) ([Sun et al., 2013](#)). In autumn and winter, values were moderate and stayed between the two extremes.  
300 However, the seasonal pattern changed above 0.6 km. Winter showed the highest depolarization ratio, while spring  
301 became the lowest. The vertical profile revealed that the change in particle shape with height strongly depends on  
302 seasons ([Wang et al., 2004](#)). In winter, the low ambient temperatures in the upper atmosphere promote the formation  
303 of non-spherical particles (e.g., ice crystals and irregular aerosols), which substantially enhance the depolarization  
304 ratio due to their anisotropic light-scattering properties ([Haarig et al., 2017](#); [Wang et al., 2021](#); [Yu et al., 2021](#)). In  
305 addition, elevated aerosol layers were dominated by long-range transported dust with pronounced nonspherical  
306 properties. However, aerosols in the upper layer were more spherical and less influenced by dust in spring ([Wang et](#)  
307 [al., 2020b](#)).

308

309



310

311 **Figure 4.** Seasonal variation of vertical aerosol (a) extinction coefficient and (b) depolarization profiles at 532 nm  
 312 from LiDAR measurements. The whiskers represent the 90th and 10th percentiles, respectively. The shaded areas  
 313 represent the 25th-75th percentiles. The connected lines depict the trend of mean values across different heights.

314

315 The extinction coefficients at 535 nm exhibited clear differences between polluted and clean days for both PM<sub>2.5</sub>  
 316 and PM<sub>10</sub>, with strong vertical and diurnal variation (**Fig. 5**). For PM<sub>2.5</sub>, polluted days were characterized by  
 317 significantly higher extinction values below 0.9 km, especially during the nighttime and the period from early  
 318 morning to near noon ([Wang et al., 2024](#)). This enhancement was mainly attributed to the stable boundary layer and  
 319 limited vertical mixing during the night, which favored the accumulation of aerosols near the surface. Strong solar  
 320 radiation enhances photochemical reactions, leading to substantial secondary aerosol formation at noon and a lift in  
 321 altitude (**Fig. 5a**). However, extinction values near the surface (below 0.4 km) were relatively low during 12:00-15:00  
 322 (BJT), with high values concentrated mainly around 0.6 km, which was consistent with the low ground-based PM<sub>2.5</sub>  
 323 concentrations during this period shown in **Fig. 3**. The lagged effect of boundary layer development indicated that  
 324 pollutants accumulated in the morning were not yet fully dispersed (**Fig. 5a**) ([Wang et al., 2024](#)). During this period,  
 325 extinction values rose not only near the surface but also extended vertically up to around 0.6 km. The upward  
 326 expansion of aerosols was driven by boundary layer development and persistent emission sources ([Dai et al., 2020](#)).

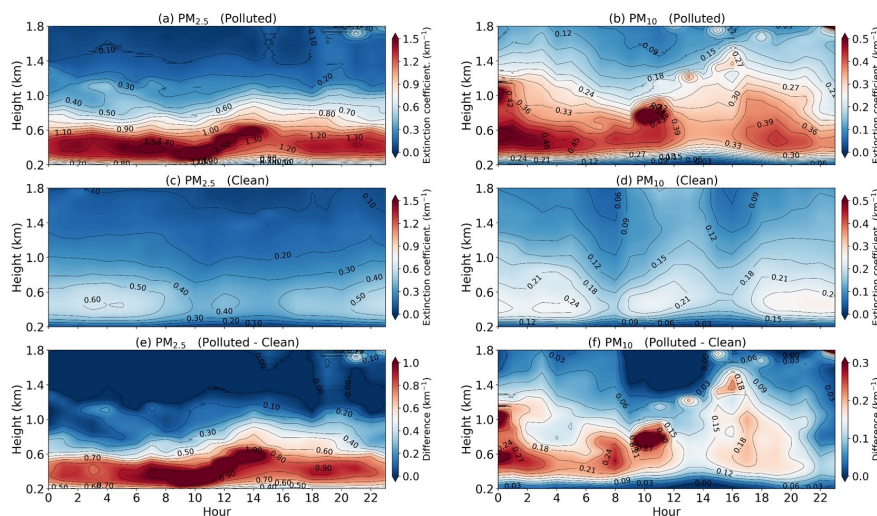


327 In contrast, clean days showed low extinction values throughout the day, with little vertical variation and no  
328 significant peak. For  $PM_{10}$ , extinction coefficients at 532 nm were also increased on polluted days (**Fig. 5b**). However,  
329 the enhancement of extinction values extended to a higher altitude compared to that of  $PM_{2.5}$ , reaching up to 1.2 km.  
330 The primary increase occurred during the night and early morning, with a minor secondary rise observed around  
331 midday ([Li et al., 2020](#)). Clean-day extinction remained uniformly low with minimal temporal variation (**Fig. 5d**).

332 For the depolarization ratio (532 nm), distinct patterns also emerged between polluted and clean days for both  
333  $PM_{2.5}$  and  $PM_{10}$  (**Fig. 6**). For  $PM_{2.5}$ , depolarization ratios near the surface (below  $\sim 0.6$  km) were relatively low on  
334 polluted days, particularly during nighttime and early morning (**Fig. 6a**). This can be attributed to the accumulation  
335 of fine, spherical particles in the stable boundary layer, which tend to have lower depolarization ratios. As altitude  
336 increased, depolarization ratios rose. This indicates the presence of more irregularly shaped or coarser particles aloft,  
337 possibly from transported dust or aged aerosols. In contrast, clean days showed uniformly low depolarization ratios  
338 across most heights, consistent with the dominance of fine, spherical aerosols under favorable dispersion conditions  
339 (**Fig. 6c**). For  $PM_{10}$ , depolarization ratios at 532 nm on polluted days exhibited a different behavior (**Fig. 6b**). Starting  
340 around 8:00 (BJT), elevated depolarization values were observed across a broad vertical layer, extending up to  $\sim 1.2$   
341 km throughout the day. This suggests that coarser particles, which typically have higher depolarization ratios, were  
342 more effectively mixed vertically and persisted at higher altitudes compared to  $PM_{2.5}$ . The broader vertical  
343 distribution of  $PM_{10}$  depolarization signals reflects the larger size and potentially different sources (e.g., resuspended  
344 dust, industrial emissions) of these particles, which are less confined by boundary layer dynamics than finer  $PM_{2.5}$ .

345 The difference between polluted and clean days highlighted a strong increase in near-surface extinction during  
346 early morning on polluted days, indicating suppressed vertical mixing and increased emission accumulation (**Fig.**  
347 **5e&f**). For  $PM_{2.5}$ , the differences were concentrated near the ground, especially below 0.9 km. The strongest  
348 enhancement appeared between 7:00 and 14:00 (BJT). A subtle lifting with height was observed around midday.  
349 Noon solar radiation maximizes surface heating, which causes severe thermal convection. The lower atmosphere  
350 becomes unstable as a result of the hot Earth transferring energy upward. It could break the stable stratification and  
351 drive upward air motion. Pollutants trapped near the surface are lifted, reducing extinction in the lower layer ( $<0.4$   
352 km) while increasing it aloft as vertical mixing intensifies ([Wang et al., 2024](#)). For  $PM_{10}$ , the enhancement tended to  
353 be localized and less vertically extended. The coarse particles may be lifted in upstream source regions, but their  
354 vertical transport weakens significantly along the trajectory. As a result, the transport altitude of  $PM_{10}$  reaching Hefei  
355 was largely confined below 1.2 km ([Shim et al., 2022](#)). Compared to  $PM_{2.5}$ , the high-value region for  $PM_{10}$  on polluted  
356 days has a higher vertical extension, and the period of strong extinction is shorter. The particles of  $PM_{10}$  are relatively

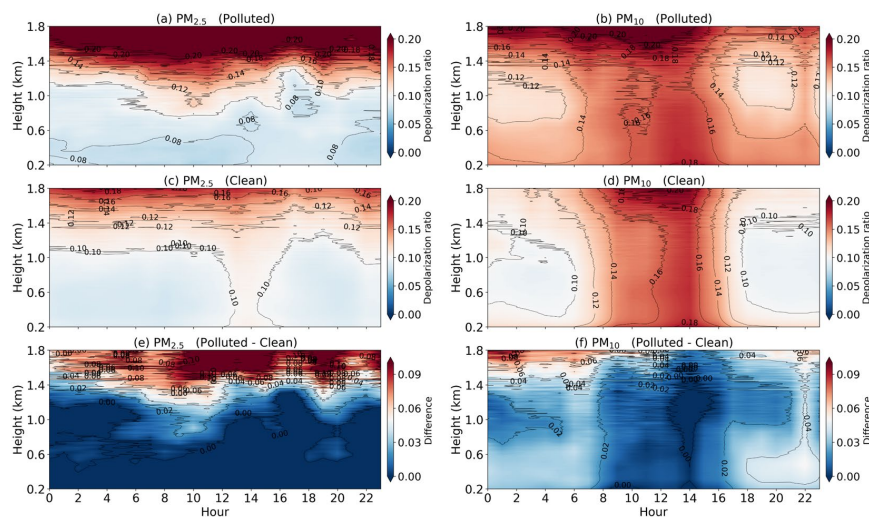
357 large and heavy, which leads to rapid sedimentation and thus a short duration of heavy pollution. Pollutants tend to  
358 accumulate in the middle and low altitudes (0.4-1.2 km) on polluted days.



359

360 **Figure 5.** Diurnal variation in the vertical distribution of aerosol extinction coefficient (Winter days for PM<sub>2.5</sub>: First  
361 column; Spring days for PM<sub>10</sub>: Second column) under days with (a, b) polluted, (c, d) clean, and (E, F) the difference  
362 between the two. All data are presented in Beijing time (BJT = UTC + 8 h) for the 532 nm channel.

363



364

365 **Figure 6.** Same as Fig. 5, but for depolarization ratio.

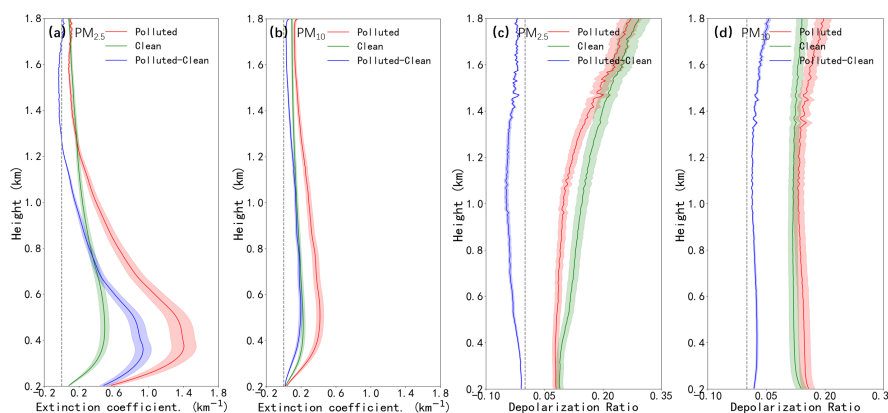
366



367 To further analyzed the vertical aerosol properties under different pollution levels, the mean extinction  
368 coefficient and depolarization ratio at 532 nm were calculated across three representative conditions (**Fig. 7**). Unlike  
369 the temporal variation that emphasized vertical profile distributions (**Fig. 5&6**), these curves highlight altitude-related  
370 trends (e.g., gradual changes, peak positions, and inflection points) for the comparison between polluted, clean, and  
371 difference conditions. For  $PM_{2.5}$ , the extinction coefficient decreased exponentially with height and intensified  
372 sharply below 0.4 km on polluted days (**Fig. 7a**) ([Wang et al., 2020a](#)). The near-surface value reached up to  $1.4 \text{ km}^{-1}$   
373 at 0.4 km, which was nearly three times higher than that on clean days. The difference was most significant within  
374 the boundary layer, especially between 0.3-0.6 km. For  $PM_{10}$  (**Fig. 7b**), although the overall extinction values were  
375 lower than those of  $PM_{2.5}$ , the difference between polluted and clean days remained obvious. The polluted-clean  
376 difference for  $PM_{10}$  was more confined below 1.2 km. This discrepancy may be attributed to that the coarse-mode  
377 particles tend to concentrate closer to the surface due to their limited vertical transport.

378 The vertical distributions of the depolarization ratio under different pollution levels are presented in **Figs. 7**  
379 (**c&d**) for  $PM_{2.5}$  and  $PM_{10}$ , respectively. For  $PM_{2.5}$ , the depolarization ratio on clean days was higher than that on  
380 polluted days across the entire vertical column up to 1.8 km (**Fig. 7c**). The depolarization ratio of  $PM_{2.5}$  increases  
381 with height. The most significant difference in depolarization ratios between polluted and clean days was observed  
382 around 1 km. Above this height, the difference narrowed but clean days still showed slightly higher values. Unlike  
383 near-surface  $PM_{2.5}$ , which is dominated by local pollution sources,  $PM_{2.5}$  at higher altitudes is mainly associated with  
384 long-range transport in the free troposphere, leading to higher depolarization ratios. Higher altitudes have more  $PM_{2.5}$   
385 particles from long-range transport in the free troposphere, which possess higher depolarization ratios ([Vakkari et al.,](#)  
386 [2021](#); [Wang et al., 2021](#)). Even at higher altitudes, the residual influence of cleaner, non-spherical particle sources in  
387 the background air kept the clean-day depolarization ratio higher ([Li et al., 2020](#)). For  $PM_{10}$ , the depolarization ratio  
388 of polluted days was higher than that of clean days across the entire vertical range (**Fig. 7d**), reflecting a greater  
389 abundance of coarse-mode and irregularly shaped particles on polluted days. Below 1.2 km, the depolarization ratio  
390 of  $PM_{10}$  was distinctly higher than that of  $PM_{2.5}$  on polluted days. This difference emphasized the dominant influence  
391 of coarse, non-spherical particles (e.g., dust and mechanically suspended material) in the  $PM_{10}$  fraction, particularly  
392 near the surface ([Shim et al., 2022](#)). On  $PM_{10}$ -polluted days in autumn, the depolarization ratio increased with height,  
393 which is mainly also affected by the long-distance transport of dust in the free troposphere.

394



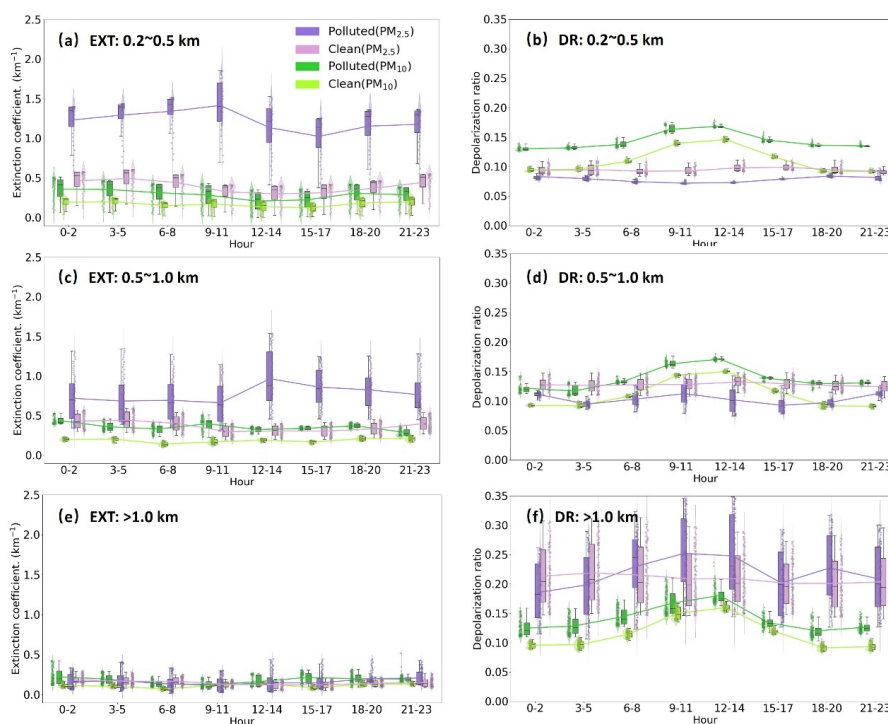
395

396 **Figure 7.** Vertical profiles of aerosol (a, b) extinction coefficient and (c, d) depolarization ratio at 532 nm for (a, c)  
 397 PM<sub>2.5</sub> in winter and (b, d) PM<sub>10</sub> in spring on polluted, clean days, and the difference between the two. The gray  
 398 dashed line represents the zero line. Note: The extinction coefficient and depolarization ratio of individual polluted  
 399 and clean days are positive physical quantities. Negative values in the "Polluted-Clean" panels indicate that the  
 400 aerosol optical parameters (extinction coefficient or depolarization ratio) are higher on clean days than on polluted  
 401 days. All data are presented in Beijing time (BJT = UTC + 8 h) for the 532 nm channel.

402

403 **Figure 8** presents the 3-hourly variation of extinction coefficient and depolarization ratio at 532 nm on polluted  
 404 and clean days across three altitude layers (0-0.5 km, 0.5-1 km, and 1-1.8 km). Below 0.5 km, the extinction  
 405 coefficients were markedly higher on polluted days for PM<sub>2.5</sub> than that on clean days, with peak values occurring at  
 406 03:00-12:00 (BJT) (**Fig. 8a**), which was consistent with the variation in surface pollutant concentrations (**Fig. 3**). The  
 407 depolarization ratio for PM<sub>2.5</sub> was lower on polluted days in contrast with clean days. This is due to the dominance  
 408 of spherical fine particles (e.g., sulfates, organic aerosols) from anthropogenic and secondary sources (**Fig. 8a&c**).  
 409 These particles scatter light less directionally compared to the irregular coarse particles (e.g., dust) prevalent on clean  
 410 days. In contrast, both the extinction coefficient and depolarization ratio for PM<sub>10</sub> were high on polluted days ([Zhang](#)  
 411 [et al., 2020a](#)). At the layer between 0.5 and 1 km, the extinction coefficient for PM<sub>2.5</sub> showed a significant peak  
 412 around 12:00 to 15:00 (BJT) on polluted days, which was consistent with the upward transport of pollutants to around  
 413 0.6 km during the same period as shown in the diurnal vertical structure (**Fig. 5**). The extinction values decreased  
 414 significantly and showed limited diurnal variability above 1 km (**Fig. 8e**). However, the depolarization ratio remained  
 415 relatively high during polluted periods. The depolarization ratio for on days in winter was higher than that of spring,  
 416 mainly because PM<sub>2.5</sub> pollution contains a higher proportion of irregular particles from coal-fired fly ash and

417 industrial emissions (Fig. 8f). The low temperatures inhibit the diffusion and settlement of coarse particles. In contrast,  
 418 days in spring for PM<sub>10</sub> pollution were more affected by coarse particles such as windblown dust. Although these  
 419 particles are irregular in shape, their large particle size makes them prone to settling. Moreover, the strong  
 420 atmospheric fluidity in spring led to a slightly lower depolarization ratio compared to winter. Overall, the greatest  
 421 contrast between polluted and clean days was observed in the lowest layer, where both particle concentration and  
 422 shape varied most distinctly with pollution level and time of day (Zhong et al., 2018).  
 423



424  
 425 **Figure 8.** Diurnal variations of (EXT: a, c, e) extinction coefficient and (DR: b, d, f) depolarization ratio at 532 nm  
 426 on polluted and clean days for PM<sub>2.5</sub> and PM<sub>10</sub> at (a, b) 0.2-0.5 km, (c, d) 0.5-1.0km, and (e, f) above 1.0 km,  
 427 respectively. The whiskers represent the 90th and 10th percentiles, respectively. The shaded areas represent the 25th-  
 428 75th percentiles. The connected lines depict the trend of mean values across different heights. All data are presented  
 429 in Beijing time (BJT = UTC + 8 h) for the 532 nm channel.

430

### 431 3.3 Role of aerosol extinction coefficient and depolarization ratio at different altitudes on 432 ground-based PM<sub>2.5</sub> and PM<sub>10</sub>

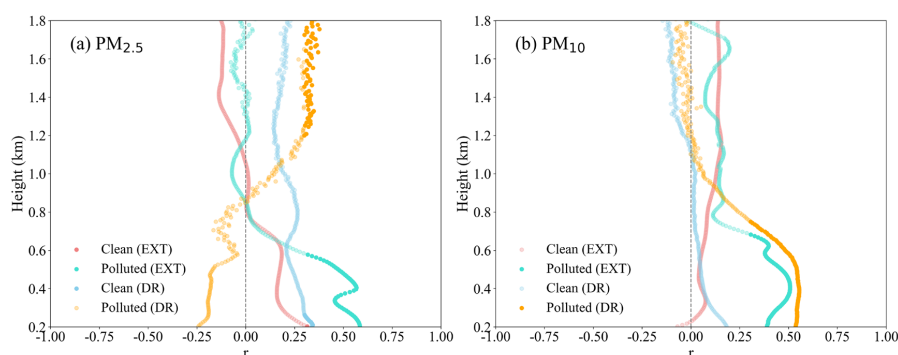
433 **Figure 9** shows the vertical profiles of the relationships between surface pollutant concentrations and aerosol



434 optical properties (extinction coefficient and depolarization ratio at 532 nm) on polluted and clean days. For PM<sub>2.5</sub>,  
 435 the extinction coefficients showed a clear positive correlation with surface PM<sub>2.5</sub> concentration throughout the profile  
 436 below 0.9 km on polluted days, marking a key boundary for vertical variation in particle composition (**Fig. 9a**). The  
 437 values on polluted days increase sharply near the surface, suggesting a local accumulation. On polluted days with  
 438 PM<sub>2.5</sub>, the depolarization ratio was negatively correlated with PM<sub>2.5</sub> concentration below 0.9 km, with fine particulate  
 439 matter dominating. As the proportion of fine particulate matter increased, the proportion of spherical particles rose,  
 440 leading to reduced depolarization ([Zhang et al., 2020a](#)). In contrast, clean days showed a consistently positive  
 441 correlation between depolarization ratio and surface pollutants throughout the vertical profile.

442 The increased depolarization levels are linked to greater proportions of non-spherical particles, such as dust or  
 443 mechanically suspended matter ([Vakkari et al., 2021](#)). The depolarization ratio showed consistently positive  
 444 correlations with surface PM<sub>10</sub> concentration on polluted days, especially below 1.2 km (**Fig. 9b**). On clean days, the  
 445 correlation between the depolarization ratio and PM<sub>10</sub> concentration remained near zero, reinforcing that the  
 446 depolarization ratio is a distinguishing feature of coarse-mode aerosols. These results revealed the contrasting aerosol  
 447 properties between PM<sub>2.5</sub> and PM<sub>10</sub> pollution. PM<sub>2.5</sub> events were dominated by fine, spherical particles that reduce  
 448 depolarization, while PM<sub>10</sub> events were closely associated with the presence of coarse, non-spherical particles that  
 449 enhanced depolarization signals ([Biuki et al., 2022](#)).

450



451

452 **Figure 9.** Vertical distributions of correlation ( $r$ ) between aerosol optical properties (532 nm) and ground-based  
 453 pollutants (a: PM<sub>2.5</sub> in winter, b: PM<sub>10</sub> in spring) on clean and polluted days. EXT = extinction coefficient; DR =  
 454 depolarization ratio. The gray dashed line represents the zero line.

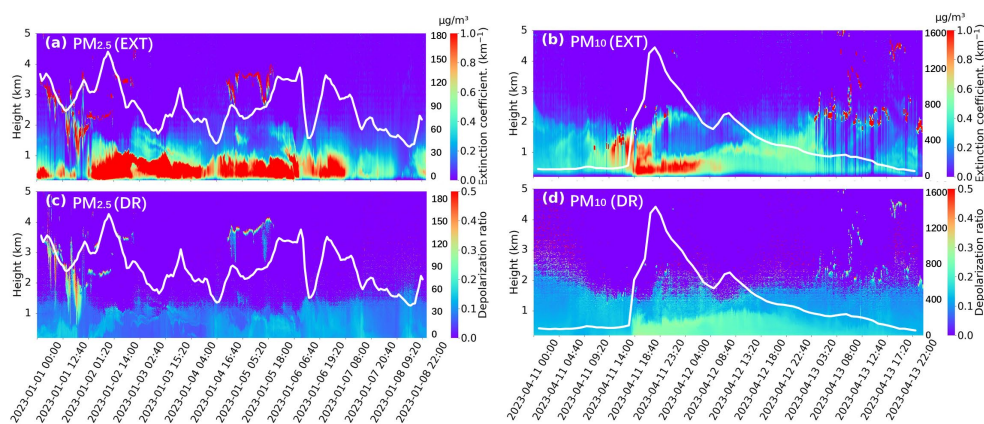
455

### 456 3.4 Analysis of LiDAR observations during heavy pollution episodes

457 Temporal variations of the extinction coefficient and depolarization ratio at 532 nm exhibited a clear association



458 with  $PM_{2.5}$  and  $PM_{10}$  concentrations, effectively highlighting severe pollution periods (**Fig. 10**). Severe  $PM_{2.5}$   
 459 pollution was evident at 10:00 a.m. on January 2, 2023 (BJT), with the maximum hourly concentration reaching  
 460  $159.6 \mu\text{g}/\text{m}^3$ . The peak of the extinction coefficient matched the actual maximum concentration of  $PM_{2.5}$ , with fine  
 461 particulate matter exhibiting strong light-scattering properties at this time (**Fig. 10a**). However, the depolarization  
 462 ratio of  $PM_{2.5}$ -polluted days showed reduced values during this peak period (**Fig. 10c**). A dramatic peak in  $PM_{10}$   
 463 concentration was observed, with the highest hourly value of  $1440 \mu\text{g}/\text{m}^3$  recorded at 22:00 p.m. (BJT) on April 11,  
 464 2023. The severe  $PM_{10}$  event was reflected by a pronounced increase in the extinction coefficient (**Fig. 10b**) ([Sun et](#)  
 465 [al., 2013](#)). In addition, the depolarization ratio exhibited high values during this period, which aligned with the  
 466 elevated extinction coefficient and was consistent with the irregular morphology of coarse particles that contributed  
 467 to both stronger light scattering and greater depolarization (**Fig. 10d**). Overall, the profiles of the extinction  
 468 coefficient and depolarization ratio correspond directly to the temporal patterns of  $PM_{2.5}$  (January 1–8, 2023) and  
 469  $PM_{10}$  (April 11–13, 2023) concentrations (**Fig. 10**). Peaks in pollutant concentrations were reflected in enhanced  
 470 extinction coefficients and characteristic depolarization ratio patterns ([Zhong et al., 2018](#)). This confirms that these  
 471 optical metrics effectively identify severe pollution episodes.  
 472



473  
 474 **Figure 10.** Pollution Episodes: Temporal dynamics of (a, b) extinction and (c, d) depolarization parameters for the  
 475 532 nm channel during severe (a, c)  $PM_{2.5}$  (January 1–8, 2023) and (b, d)  $PM_{10}$  (April 11–13, 2023) periods in Hefei.  
 476 The white lines represent the hourly (a)  $PM_{2.5}$  and (b)  $PM_{10}$  concentrations, with their scale on the secondary y-axis.  
 477 All data are presented in Beijing time (BJT = UTC + 8 h). EXT = extinction coefficient; DR = depolarization ratio.  
 478

### 479 3.5 Analysis of meteorological conditions and their driving role in air pollution

480 **Figure S1** shows boxplots of the concentrations of  $PM_{2.5}$  and  $PM_{10}$  in temperature (T), relative humidity (RH),



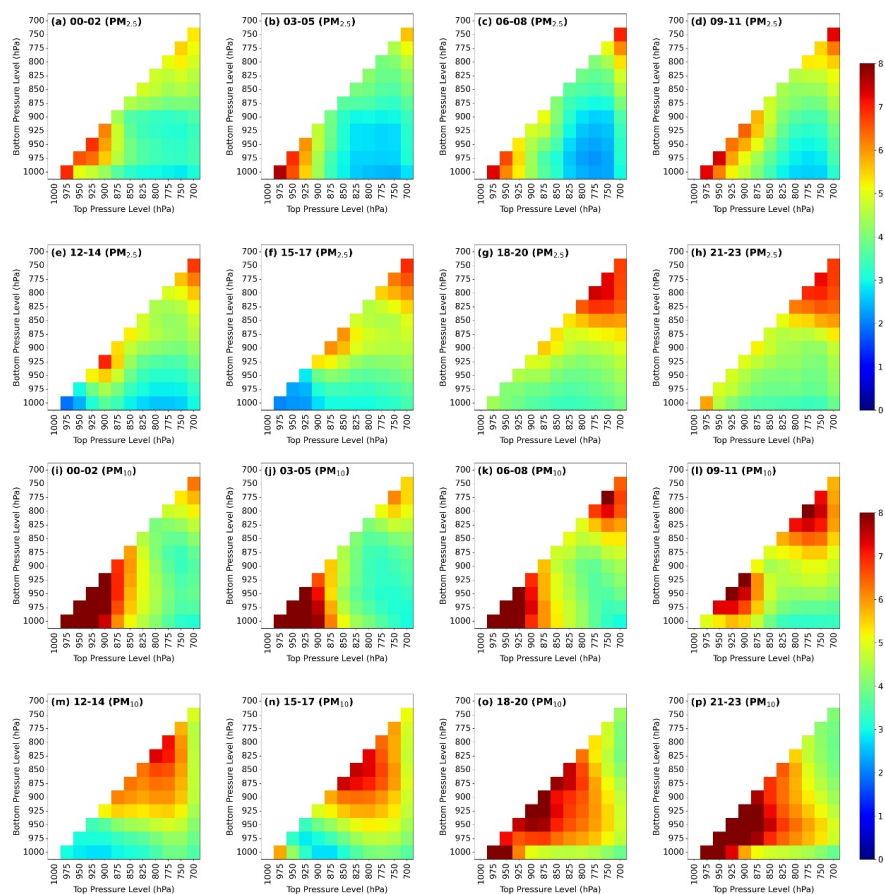
481 surface pressure (PRS), and wind speed (WS) bins, respectively. Overall, the relationships of temperature with PM<sub>2.5</sub>,  
482 PM<sub>10</sub> were not significant (**Fig. S1a&e**). The RH exerted distinct influences on PM<sub>10</sub> and PM<sub>2.5</sub> concentrations (**Fig.**  
483 **S1b&f**). Higher PM<sub>2.5</sub> concentrations were associated with increased RH, primarily due to elevated humidity  
484 promoting the condensation of gaseous precursors (e.g., sulfur dioxide, nitrogen oxides) onto pre-existing PM<sub>2.5</sub>  
485 particles (**Fig. S1b**) ([Wang et al., 2004](#)). Additionally, it accelerated secondary aerosol formation via aqueous-phase  
486 chemical reactions in the atmosphere, thereby elevating PM<sub>2.5</sub> levels ([Yang et al., 2022](#)). In contrast to PM<sub>2.5</sub>, the  
487 relationship between PM<sub>10</sub> concentrations and RH was inverse (**Fig. S1f**). Higher RH drives coarse particles like  
488 PM<sub>10</sub> to absorb moisture, grow in size, and then settle out of the atmosphere more easily. It may also enhance wet  
489 deposition processes such as rain or fog scavenging, reducing their airborne concentrations ([Gao et al., 2020](#); [Ma et](#)  
490 [al., 2023](#)). PRS tended to increase with rising concentrations of PM<sub>2.5</sub> and PM<sub>10</sub> (**Fig. S1c&g**). The average pressure  
491 values were lower on clean days (PM<sub>2.5</sub> ≤ 75, PM<sub>10</sub> ≤ 150) and became higher on polluted days. The high-pressure  
492 systems promote atmospheric stability and suppress vertical mixing, thereby facilitating the accumulation of  
493 particulate matter near the surface ([Li et al., 2015](#)). Wind speed exhibited a decreasing trend with increasing PM<sub>2.5</sub>  
494 concentrations (**Fig. S1d&h**). Lower wind speeds during heavy pollution periods indicate weak horizontal dispersion,  
495 which contributes to the persistence and accumulation of fine particles in the boundary layer. In addition, the polar  
496 plot of PM<sub>2.5</sub> concentrations shows a directional pattern, with the highest values predominantly associated with winds  
497 from the northwest (**Fig. S2a**). The cities of northern Anhui, Henan, and even further north were characterized by  
498 dense industrial activities and frequent wintertime heating emissions, which contribute to elevated PM<sub>2.5</sub> levels ([Qian](#)  
499 [et al., 2024](#); [Shi et al., 2018](#)). For PM<sub>10</sub>, the concentration distribution was more spatially confined but still shows a  
500 dominant contribution from the northwest area ([Huang et al., 2016](#)). The most intense PM<sub>10</sub> concentrations were  
501 clustered in the northwest, appearing localized and patchy (**Fig. S2b**). This may reflect the influence of transport and  
502 mechanical resuspension processes, such as road dust and construction activities.

503 VWS is a key dynamic factor affecting pollutant dispersion, as it influences mechanical turbulence and vertical  
504 mixing within the boundary layer ([Deng et al., 2023](#)). **Figures 11** and **12** illustrate the diurnal variation of VWS on  
505 polluted and clean days, respectively. For PM<sub>2.5</sub>, weak shear persisted throughout the boundary layer on polluted days  
506 when temperature inversions and stable stratification typically dominate the lower atmosphere (**Fig. 11a-h**). Clean  
507 days showed stronger shear during most periods, enhancing upward transport and dilution of fine particles (**Fig. 12**).  
508 Notably, the difference in VWS between polluted and clean days WAS more pronounced in the lower boundary layer  
509 (1000–900 hPa) than in the upper boundary layer (875–700 hPa) ([Zhang et al., 2020b](#)). Hence, suppressed vertical  
510 mixing near the surface contributed significantly to the accumulation of PM<sub>2.5</sub>. Surface air quality tends to deteriorate



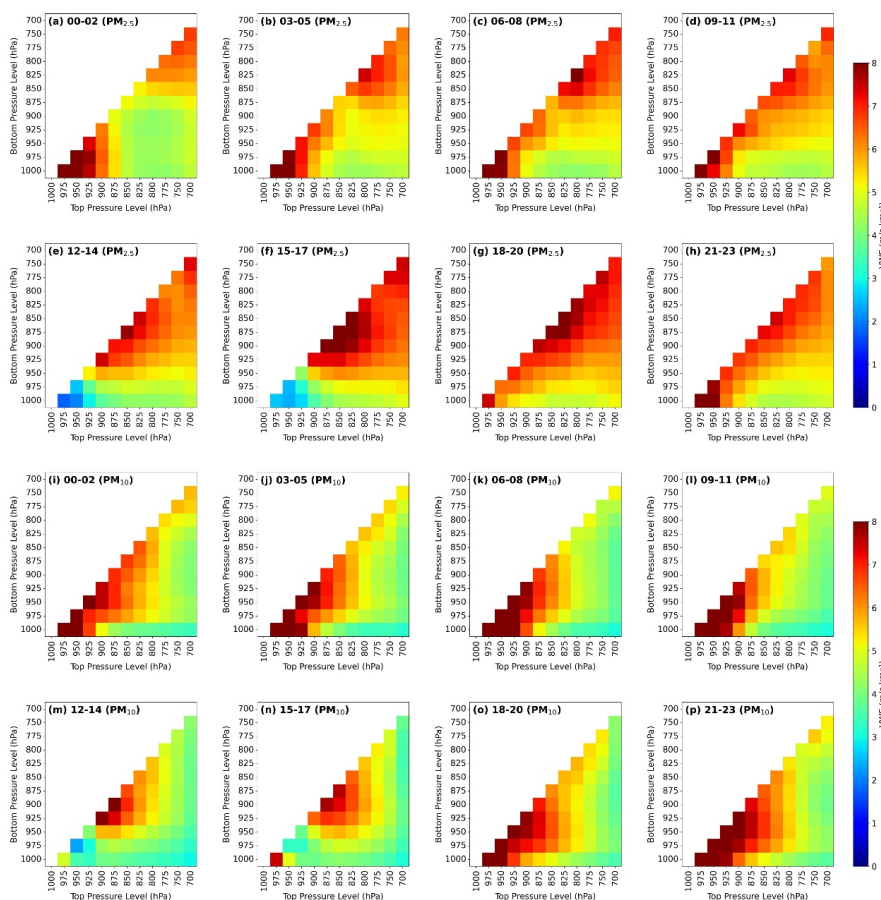
511 significantly due to pollutant accumulation near the ground, especially in cases where shear is insufficient in the  
512 lower layer ([Wang et al., 2024](#)), which was consistent with the trend that the extinction coefficient at 532 nm near the  
513 surface is higher than that in the upper layer (**Figs. 7 & 8**).

514 Contrary to the expectation that polluted days generally exhibited weak VWS, the VWS associated with  $PM_{10}$   
515 on polluted days was not consistently lower than that on clean days (**Fig. 11 i-p, Fig. 12 i-p**). In particular, dust storms  
516 with high  $PM_{10}$  levels are typically accompanied by intensified VWS, which is conducive to dust uplift and transport  
517 under dynamic atmospheric conditions ([Yang et al., 2019](#)). The large VWS associated with  $PM_{10}$  would clear the air  
518 in the upper air at the beginning but later contributed to raising surface  $PM_{10}$  levels through regional transport at the  
519 near-surface and through downward transport of aerosol particles from the upper air. During the onset phase of dust  
520 intrusion, intensified shear facilitates both horizontal and vertical transport of dust particles ([Biuki et al., 2022](#)). From  
521 00:00 am to 11:00 (BJT), the VWS in the upper layer (850 hpa-700 hpa) gradually increases on  $PM_{2.5}$ -polluted days.  
522 At night, the near-surface air cools, forming a stable temperature inversion layer that inhibits vertical mixing. Hence,  
523 the stable structure would lead to weak VWS in the upper layer. As the sun rises in the mornings, the inversion layer  
524 gradually dissipates, and vertical mixing shifts from being suppressed to active (**Fig. 11 i-l**). The VWS in the upper  
525 layer gradually increases due to the mixing effect. In addition,  $PM_{10}$  pollution often occurs during cold front passage.  
526 The vertical gradient of wind direction and speed changes suddenly near the frontal surface when cold and warm air  
527 masses converge. Once the front is located in a certain pressure range, the wind shear may be significantly higher  
528 than that in the surrounding layers. The weaker VWS between adjacent pressure layers (e.g., near 825–850 hPa) may  
529 correspond to the fault distribution (**Fig. 11 i-l**). The sinking of cold air also leads to an increase in VWS at the lower  
530 level.



531

532 **Figure 11.** Three-hourly variation of vertical wind shear for (a-h)  $PM_{2.5}$  and (i-p)  $PM_{10}$  on polluted days in Hefei,  
 533 presented as 3-hourly intervals (a&i: 00:00–02:00 BJT, b&j: 03:00–05:00 BJT, c&k: 06:00–08:00 BJT, d&l: 09:00–  
 534 11:00 BJT, e&m: 12:00–14:00 BJT, f&n: 15:00–17:00 BJT, g&o: 18:00–20:00 BJT, h&p: 21:00–23:00 BJT). Beijing  
 535 Time (BJT) is UTC+8, the local standard time used in this study. The axes indicate the vertical bounds (upper and  
 536 lower pressure levels) used to compute VWS, where the main diagonal (from top-right to bottom-left) corresponds  
 537 to self-referential values for single-layer calculations. The color gradient represents the magnitude of VWS between  
 538 adjacent atmospheric layers.



539

540 **Figure 12.** Same as Fig. 11, but under clean days.

541

542 To clarify the synoptic influences on PM<sub>2.5</sub> and PM<sub>10</sub> pollution, we analyzed the distributions of air temperature  
 543 across different pressure levels from March 2021 to May 2023. During PM<sub>2.5</sub> pollution days, temperatures at all levels  
 544 were consistently higher than those on clean days. The warming showed a notable pattern, with the most pronounced  
 545 trend initially observed at 875 hPa, (Fig. 13b). The enhanced upper-level warming relative to the lower-level led to  
 546 a thermally stable stratification, which inhibited vertical mixing and promoted the accumulation of PM<sub>2.5</sub> near the  
 547 surface. In contrast, PM<sub>10</sub>-polluted days exhibited negative temperature differences below 875 hPa (Fig. 13d),  
 548 indicating the intrusion of cold air masses. These cold air masses, often accompanied by long-range dust transport,  
 549 not only bring in PM<sub>10</sub> particles from upwind regions but also suppress vertical mixing in the lower atmosphere due  
 550 to their higher density. Notably, the altitude of the cooling (875 hPa) coincided with the effective aerosol layer height  
 551 identified in our LiDAR-based analyses (Figs. 8, 11, 12), which supported the conclusion that dust particles were



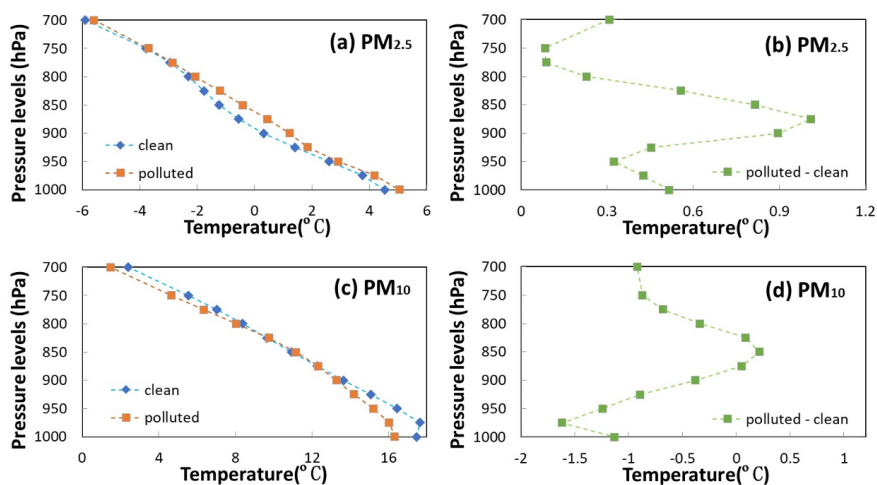
552 primarily transported within this level.

553 To further investigate the vertical thermal and humidity differences between clean and polluted days, we focus  
554 on three key pressure levels (1000, 850, and 500 hPa). During PM<sub>2.5</sub>-polluted periods, the warming at 850 hPa was  
555 greater than that near the surface at 1000 hPa in Hefei (**Fig. S3f&i**). This vertical temperature structure created a  
556 pronounced inversion, which inhibited the vertical mixing and enhanced the atmospheric stability. The lower  
557 troposphere also exhibited elevated relative humidity, particularly in Hefei and nearby regions. Elevated relative  
558 humidity suppresses turbulent exchange and reduces dilution capacity, and hence forms a shallow, moist, and stable  
559 boundary layer that favors pollutant persistence and contributes to poor air quality. In contrast, the clean days showed  
560 a lower humidity in the boundary layer and a weaker vertical temperature gradient, allowing enhanced upward motion  
561 and effective removal of surface aerosols ([Deng et al., 2023](#)). PM<sub>10</sub> pollution episodes occurred under a markedly  
562 different meteorological background (**Fig. S4**). Specifically, the relative humidity at both 1000 hPa and 850 hPa was  
563 significantly lower on PM<sub>10</sub>-polluted days than on clean days (**Fig. S4f&i**). Aloft cold air intrusions occurred on PM<sub>10</sub>  
564 pollution days, creating favorable conditions for the large-scale transport of dust into Hefei. Under such dry and calm  
565 conditions, PM<sub>10</sub> accumulation is likely driven by mechanical resuspension or regional dust transport rather than  
566 secondary aerosol formation processes enhanced by moisture ([Li et al., 2020](#)). Overall, these findings reveal that  
567 PM<sub>2.5</sub> episodes over Hefei are typically governed by moist and thermodynamically stable boundary layers under  
568 subsiding air masses, while PM<sub>10</sub> events are more influenced by dust-laden airflow and dry boundary-layer dynamics.  
569 The distinct thermal and humidity structures observed across the vertical profile emphasize the importance of  
570 differentiating pollution types when diagnosing meteorological drivers.

571 The vertical wind velocity was investigated at three pressure levels to reveal the dynamic mechanisms on PM<sub>2.5</sub>  
572 and PM<sub>10</sub> pollution days (**Figs. 14 & 15**). On PM<sub>2.5</sub>-polluted days, the atmosphere around Hefei exhibits a clear  
573 subsidence trend at 850 and 1000 hPa (**Fig. 14**). The subsidence reflects the existence of high-pressure systems and  
574 stagnant synoptic conditions, which contribute to the accumulation of fine particles. This inhibition of the upward  
575 motion of vertical wind corresponds with a stable thermal structure, which can effectively restrict vertical exchange  
576 and compress the boundary layer. During PM<sub>10</sub> pollution events, subsidence at 500 hPa is significantly greater than  
577 on clear days compared to clean days (**Fig. 15**). However, Hefei is located in a unique region defined by  
578 upward motion at 850 hPa, with a comparable weak upward movement also observed at 1000 hPa. The subsidence  
579 at 500 hPa stabilizes the atmosphere and suppresses the upward dispersion of particles. Meanwhile, upward motion  
580 at 850 hPa and near the surface (1000 hPa) may be caused by local convergence or orographic lifting, allowing the  
581 uplift and recirculation of dust within the lower troposphere. This dynamic difference could reflect more complex



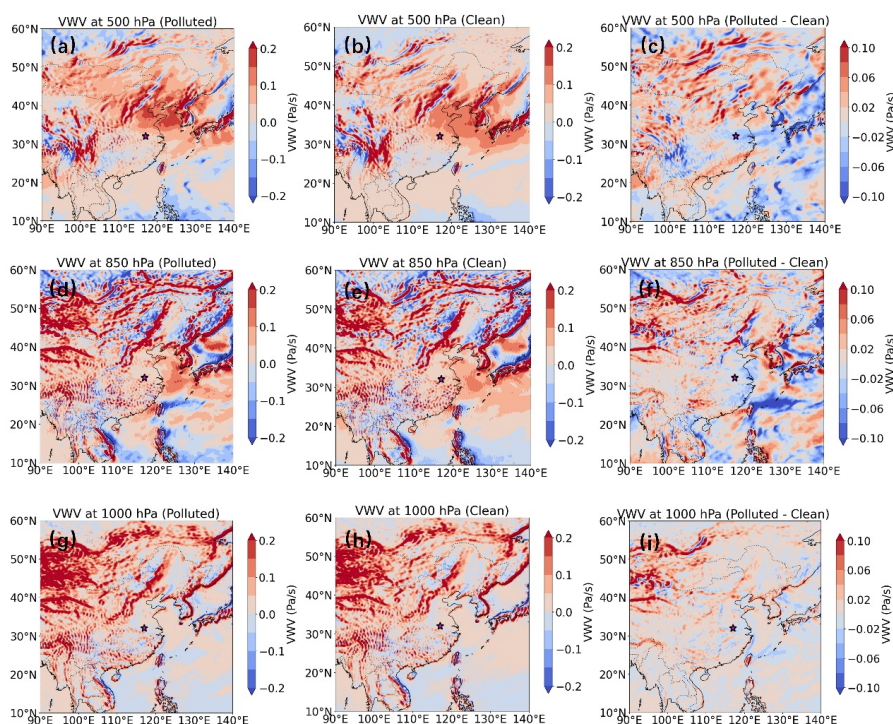
582 interactions between local surface sources and large-scale synoptic. Upward motion at 850 hPa supports the  
583 interpretation that  $PM_{10}$  events are influenced by weak convective movements or vertical recycling of particles within  
584 a confined layer rather than stagnation alone. These findings reveal that  $PM_{2.5}$  and  $PM_{10}$  pollution in Hefei are  
585 governed by contrasting vertical dynamic regimes.  $PM_{2.5}$  events are closely tied to a uniformly subsiding atmosphere,  
586 which favors the trapping and accumulation of fine particles. In contrast,  $PM_{10}$  events are characterized by a layered  
587 structure, where upper-level subsidence and lower-level ascent work in tandem to recirculate coarse particles, rather  
588 than simply trapping them. This distinction underscores the need for targeted, pollutant-specific strategies in air  
589 quality forecasting and management.



590

591 **Figure 13.** Vertical distributions of temperature for polluted, clean, and their difference in (a, b)  $PM_{2.5}$  and (c, d)

592  $PM_{10}$ .

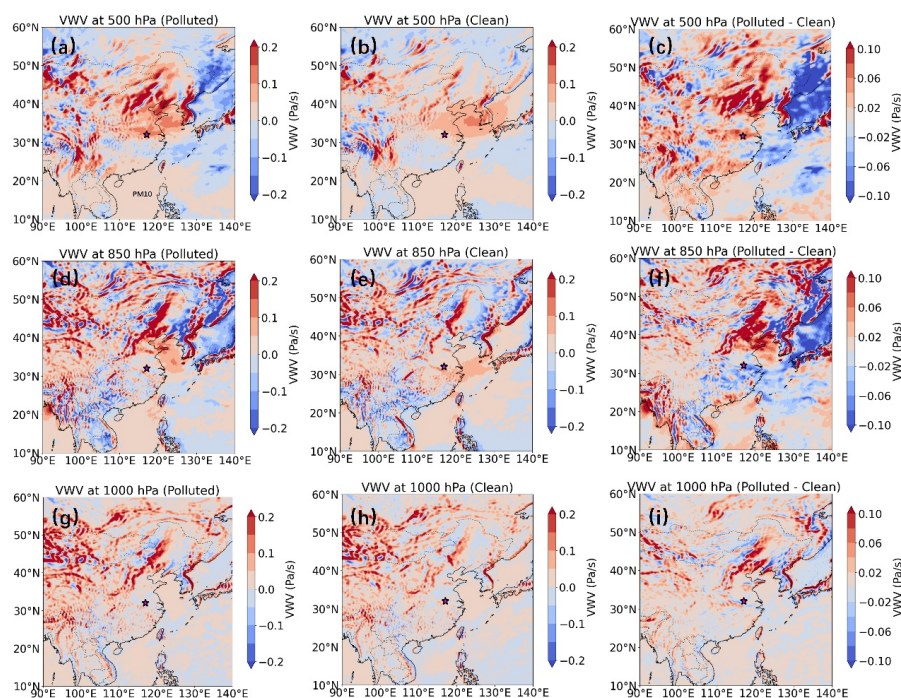


593

594 **Figure 14.** Spatial distribution of the vertical wind velocity (VWV) at three pressure levels (500 hPa: a–c; 850 hPa:  
595 d–f; 1000 hPa: g–i) on PM<sub>2.5</sub>-polluted (left column), clean (middle column) days and the difference between them  
596 (right column), respectively. The areas highlighted with a red star represents the location of Hefei.

597

598



599

600 **Figure 15.** Same as Fig. 14, but on PM<sub>10</sub>-polluted (left column), clean (middle column) days and the difference  
 601 between them (right column), respectively.

602

#### 603 4. Conclusions

604 This study comprehensively assesses the vertical structures of aerosols in Hefei by comparing fine (PM<sub>2.5</sub>) and  
 605 coarse (PM<sub>10</sub>) particulate matter on clean and polluted days. We utilized long-term aerosol LiDAR measurements  
 606 and reanalysis meteorological data to compare the vertical distribution characteristics of different particulate pollution  
 607 types as well as the underlying thermodynamic and dynamic mechanisms that drive their vertical development.  
 608 Aerosol extinction coefficients at 532 nm for PM<sub>2.5</sub> and PM<sub>10</sub> were consistently higher on polluted days than on clean  
 609 days. Since fine-mode particles predominate the aerosol population on PM<sub>2.5</sub> pollution days, the depolarization ratios  
 610 fell within a range lower than those observed on clean days. In contrast, PM<sub>10</sub>-polluted days had larger depolarization  
 611 ratios than clean days, indicating significant contributions from non-spherical coarse particles.

612 Our findings reveal that the accumulation of PM<sub>2.5</sub> is closely linked to stable boundary layer structures  
 613 characterized by high humidity, weak vertical shear, and a mid-level inversion temperature. These conditions  
 614 collectively inhibit vertical exchange and confine fine particles near the surface. The vertical extinction and  
 615 depolarization profiles support the dominance of aerosols during PM<sub>2.5</sub> pollution, particularly in the lower 0.9 km. In



616 contrast, PM<sub>10</sub> pollution is typically associated with low humidity and mechanically driven transport of dust from  
617 upwind sources. The vertical profiles show enhanced depolarization ratios, indicating the presence of non-spherical,  
618 coarse particles such as dust or resuspended material. Distinct vertical motion patterns identify the two types of  
619 pollution. PM<sub>2.5</sub> episodes showed upward mobility in the mid-troposphere and near-surface subsidence, which  
620 reinforced stratification and pollution trapping. However, PM<sub>10</sub> events were distinguished by upper-level subsidence  
621 coupled with low-level ascent, which might facilitate vertical transport of coarse particles during regional dust  
622 episodes. These dynamic differences highlight that PM<sub>2.5</sub> and PM<sub>10</sub> are generated by fundamentally separate  
623 atmospheric processes, and a unified treatment of particulate pollution risks oversimplifies their behavior.

624 Expanding such analyses across multiple sites would also aid in identifying geographical heterogeneity and  
625 testing the generalizability of the discovered trends. Future research may be directed toward integrating long-term,  
626 high-resolution vertical observations with advanced modeling approaches to better understand the multiscale  
627 dynamics behind various forms of particle pollution and create tailored mitigation solutions.

628

### 629 **Acknowledgments**

630 This work was supported by the Innovation and Development Special Project of Anhui Meteorological Bureau  
631 (CXB202404), the Open Fund Project for Heavy Rain (BYKJ2025D03), the Science and Technology Projects of  
632 Xizang Autonomous Region, China (XZ202502JD0041), the Special Project for Forecasters of Anhui Meteorological  
633 Bureau (KY202003), and the 2025 Independent Innovation Scientific Research Project of Anhui Public  
634 Meteorological Service Center (GFCX202504).

635

### 636 **Data Availability**

637 Hourly concentrations of major air pollutants were obtained from the China National Environmental Monitoring  
638 Centre (CNEMC) (<https://www.cnemc.cn/>). Surface meteorological variables were obtained from the China  
639 Meteorological Administration (CMA) (<http://data.cma.cn/en>). The ERA5 reanalysis dataset, used to investigate the  
640 impact of synoptic systems on PM<sub>2.5</sub> and PM<sub>10</sub> pollution, was freely accessible via the Copernicus Climate Change  
641 Services platform (<https://cds.climate.copernicus.eu/datasets>).

642

### 643 **Author Contribution**

644 X.D. conceived the study; Y.Y. acquired and analyzed the data and drafted the manuscript; R.D. and Q.X.  
645 performed data processing and investigation; Q.H., Y.L., and C.W. provided theoretical support; J.X. and Y.S.



646 discussed the results and revised the manuscript; Y.L. acquired funding; all co-authors reviewed and approved the  
647 final version of the manuscript.

648

### 649 **Competing interests**

650 The authors declare that they have no conflict of interest.

651

### 652 **References**

- 653 Ansmann, A., Mueller, D., Wandinger, U., & Mamouri, R.E. (2013). Lidar profiling of aerosol optical and microphysical  
654 properties from space: Overview, review, and outlook. In, *1st International Conference on Remote Sensing and*  
655 *Geoinformation of the Environment (RSCy)*. Paphos, CYPRUS
- 656 Biuki, Z.A., Parvin, P., & Aghaei, M. (2022). Satellite remote sensing of particulate matter in the atmosphere of megacities:  
657 A case study of Tehran, Iran. *Atmospheric Pollution Research*, 13, <https://doi.org/10.1016/j.apr.2022.101545>.
- 658 Cairo, F., Di Liberto, L., Dionisi, D., & Snels, M. (2024). Understanding aerosol-cloud interactions through lidar techniques:  
659 A review. *Remote Sensing*, 16, <https://doi.org/10.3390/rs16152788>.
- 660 Chen, C., Song, X., Wang, Z., Chen, Y., Wang, X., Bu, Z., Zhang, X., Zhuang, Q., Pan, X., Li, H., Zhang, F., Wang, X., Li,  
661 X., & Zheng, R. (2022). Calibration methods of atmospheric aerosol lidar and a case study of haze process. *Frontiers*  
662 *in Physics*, 10, <https://doi.org/10.3389/fphy.2022.942926>.
- 663 Chen, W., Tang, H.Z., Zhao, H.M., & Yan, L. (2016). Analysis of aerosol properties in Beijing based on ground-based sun  
664 photometer and air quality monitoring observations from 2005 to 2014. *Remote Sensing*, 8,  
665 <https://doi.org/10.3390/rs8020110>.
- 666 Chen, X., Yang, T., Wang, H.B., Wang, F.T., & Wang, Z.F. (2023). Variations and drivers of aerosol vertical characterization  
667 after clean air policy in China based on 7-years consecutive observations. *Journal of Environmental Sciences*, 125,  
668 499-512, <https://doi.org/10.1016/j.jes.2022.02.036>.
- 669 Chen, Y., Bu, Z., Wang, X., Dai, Y., Li, Z., Lu, T., Liu, Y., & Wang, X. (2024a). Development and calibration of 532 nm  
670 standard aerosol lidar with low blind area. *Remote Sensing*, 16, <https://doi.org/10.3390/rs16030570>.
- 671 Chen, Z., Ji, C., Mao, J., Wang, Z., Jiao, Z., Gao, L., Xiang, Y., & Zhang, T. (2024b). Downdraft influences on the  
672 differences of PM<sub>2.5</sub> concentration: Insights from a mega haze evolution in the winter of northern China.  
673 *Environmental Research Letters*, 19, <https://doi.org/10.1088/1748-9326/ad1229>.
- 674 Chouza, F., Reitebuch, O., Gross, S., Rahm, S., Freudenthaler, V., Toledano, C., & Weinzierl, B. (2015). Retrieval of aerosol  
675 backscatter and extinction from airborne coherent Doppler wind lidar measurements. *Atmospheric Measurement*



- 676 *Techniques*, 8, 2909-2926, <https://doi.org/10.5194/amt-8-2909-2015>.
- 677 Dai, F., Chen, M., & Yang, B. (2020). Spatiotemporal variations of PM<sub>2.5</sub> concentration at the neighborhood level in five  
678 Chinese megacities. *Atmospheric Pollution Research*, 11, 190-202, <https://doi.org/10.1016/j.apr.2020.03.010>.
- 679 Deng, X.L., Chen, J., Dai, R., Zhai, Z.F., He, D.Y., Zhao, L., Jin, X.L., & Zhang, J.P. (2023). The effects of planetary  
680 boundary layer features on air pollution based on ERA5 data in East China. *Atmosphere*, 14,  
681 <https://doi.org/10.3390/atmos14081273>.
- 682 Fan, G., Zhang, B., Zhang, T., Fu, Y., Pei, C., Lou, S., Li, X., Chen, Z., & Liu, W. (2024). Accuracy evaluation of differential  
683 absorption lidar for ozone detection and intercomparisons with other instruments. *Remote Sensing*, 16,  
684 <https://doi.org/10.3390/rs16132369>.
- 685 Fan, S., Gao, C.Y., Wang, L., Yang, Y., Liu, Z., Hu, B., Wang, Y., Wang, J., & Gao, Z. (2021). Elucidating roles of near-  
686 surface vertical layer structure in different stages of PM<sub>2.5</sub> pollution episodes over urban Beijing during 2004-2016.  
687 *Atmospheric Environment*, 246, <https://doi.org/10.1016/j.atmosenv.2020.118157>.
- 688 Fang, Z., Yang, H., Li, C., Kuang, Z., Xu, X., & Jin, H. (2024). Reveal persistent haze pollution episodes in Hefei: A  
689 perspective from ground-based and satellite observation. *Air Quality Atmosphere and Health*, 17, 2555-2568,  
690 <https://doi.org/10.1007/s11869-024-01587-2>.
- 691 Gao, F., Bergant, K., Filipcic, A., Forte, B., Hua, D.X., Song, X.Q., Stanic, S., Veberic, D., & Zavrtnik, M. (2011).  
692 Observations of the atmospheric boundary layer across the land-sea transition zone using a scanning Mie lidar.  
693 *Journal of Quantitative Spectroscopy & Radiative Transfer*, 112, 182-188,  
694 <https://doi.org/10.1016/j.jqsrt.2010.04.001>.
- 695 Gao, Y.-Q., Chen, Y., Liu, G.-D., & Zhang, J.-M. (2020). Investigating the influence of meteorological factors on particulate  
696 matters: A case study based on path analysis. *Energy & Environment*, 31, 479-491,  
697 <https://doi.org/10.1177/0958305x19876696>.
- 698 Garratt, J.R. (1994). Review: The atmospheric boundary layer. *Earth-Science Reviews*, 37, 89-134,  
699 [https://doi.org/10.1016/0012-8252\(94\)90026-4](https://doi.org/10.1016/0012-8252(94)90026-4).
- 700 Gebauer, H., Floutsis, A.A., Haarig, M., Radenz, M., Engelmann, R., Althausen, D., Skupin, A., Ansmann, A., Zenk, C., &  
701 Baars, H. (2024). Tropospheric sulfate from Cumbre Vieja (La Palma) observed over Cabo Verde contrasted with  
702 background conditions: A lidar case study of aerosol extinction, backscatter, depolarization and lidar ratio profiles  
703 at 355, 532 and 1064 nm. *Atmospheric Chemistry and Physics*, 24, 5047-5067, [https://doi.org/10.5194/acp-24-5047-](https://doi.org/10.5194/acp-24-5047-2024)  
704 [2024](https://doi.org/10.5194/acp-24-5047-2024).
- 705 Haarig, M., Ansmann, A., Gasteiger, J., Kandler, K., Althausen, D., Baars, H., Radenz, M., & Farrell, D.A. (2017). Dry



- 706 versus wet marine particle optical properties: RH dependence of depolarization ratio, backscatter, and extinction  
707 from multiwavelength lidar measurements during SALTRACE. *Atmospheric Chemistry and Physics*, 17, 14199-  
708 14217, <https://doi.org/10.5194/acp-17-14199-2017>.
- 709 Han, X., & Cao, T. (2022). Urbanization level, industrial structure adjustment and spatial effect of urban haze pollution:  
710 Evidence from China's Yangtze River Delta urban agglomeration. *Atmospheric Pollution Research*, 13,  
711 <https://doi.org/10.1016/j.apr.2022.101427>.
- 712 He, G., Deng, T., Wu, D., Wu, C., Huang, X., Li, Z., Yin, C., Zou, Y., Song, L., Ouyang, S., Tao, L., & Zhang, X. (2021).  
713 Characteristics of boundary layer ozone and its effect on surface ozone concentration in Shenzhen, China: A case  
714 study. *Science of the Total Environment*, 791, <https://doi.org/10.1016/j.scitotenv.2021.148044>.
- 715 He, Y., Li, L., Wang, H., Xu, X., Li, Y., & Fan, S. (2022). A cold front induced co-occurrence of O<sub>3</sub> and PM<sub>2.5</sub> pollution in  
716 a Pearl River Delta city: Temporal variation, vertical structure, and mechanism. *Environmental Pollution*, 306,  
717 <https://doi.org/10.1016/j.envpol.2022.119464>.
- 718 Huang, L., Chen, M.D., & Hu, J.L. (2016). Twelve-year trends of PM<sub>10</sub> and visibility in the Hefei metropolitan area of  
719 China. *Advances in Meteorology*, 2016, <https://doi.org/10.1155/2016/4810796>.
- 720 Jin, X., Cai, X., Yu, M., Wang, X., Song, Y., Kang, L., Zhang, H., & Zhu, T. (2021). Mesoscale structure of the atmospheric  
721 boundary layer and its impact on regional air pollution: A case study. *Atmospheric Environment*, 258,  
722 <https://doi.org/10.1016/j.atmosenv.2021.118511>.
- 723 Kumar, V.R., Collins, R.L., & Yellapragada, B.K. (2024). Polarization lidar observations of diurnal and seasonal variations  
724 in the atmospheric mixing layer above a tropical rural place gadanki, India. *Journal of Atmospheric and Solar-  
725 Terrestrial Physics*, 263, <https://doi.org/10.1016/j.jastp.2024.106335>.
- 726 Lee, K., Youngmin, N., 김관철, 이다솜, & 이광열 (2016). Estimation of surface-level PM<sub>2.5</sub> concentration based on  
727 MODIS aerosol optical depth over Jeju, Korea. *Korean Journal of Remote Sensing*, 32, 413-421,  
728 <https://doi.org/10.7780/kjrs.2016.32.5.2>.
- 729 Li, H.D., Sodoudi, S., Liu, J.F., & Tao, W. (2020). Temporal variation of urban aerosol pollution island and its relationship  
730 with urban heat island. *Atmospheric Research*, 241, <https://doi.org/10.1016/j.atmosres.2020.104957>.
- 731 Li, Q.H., Zhang, H.S., Jin, X.P., Cai, X.H., & Song, Y. (2022). Mechanism of haze pollution in summer and its difference  
732 with winter in the North China Plain. *Science of the Total Environment*, 806,  
733 <https://doi.org/10.1016/j.scitotenv.2021.150625>.
- 734 Li, X., Wang, Y., Shen, L., Zhang, H., Zhao, H., Zhang, Y., & Ma, Y. (2018). Characteristics of boundary layer structure  
735 during a persistent haze event in the central Liaoning city Cluster, Northeast China. *Journal of Meteorological*



- 736 *Research*, 32, 302-312, <https://doi.org/10.1007/s13351-018-7053-6>.
- 737 Li, Y., Chen, Q.L., Zhao, H.J., Wang, L., & Tao, R. (2015). Variations in PM<sub>10</sub>, PM<sub>2.5</sub> and PM<sub>1.0</sub> in an urban area of the  
738 Sichuan basin and their relation to meteorological factors. *Atmosphere*, 6, 150-163,  
739 <https://doi.org/10.3390/atmos6010150>.
- 740 Li, Y., Huang, T., Lee, H.F., Heo, Y., Ho, K.-F., & Yim, S.H.L. (2024). Integrating Doppler lidar and machine learning into  
741 land-use regression model for assessing contribution of vertical atmospheric processes to urban PM<sub>2.5</sub> pollution.  
742 *Science of the Total Environment*, 952, <https://doi.org/10.1016/j.scitotenv.2024.175632>.
- 743 Liu, C., Huang, J., Wang, Y., Tao, X., Hu, C., Deng, L., Xu, J., Xiao, H.-W., Luo, L., Xiao, H.-Y., & Xiao, W. (2020).  
744 Vertical distribution of PM<sub>2.5</sub> and interactions with the atmospheric boundary layer during the development stage of  
745 a heavy haze pollution event. *Science of the Total Environment*, 704,  
746 <https://doi.org/10.1016/j.scitotenv.2019.135329>.
- 747 Liu, J.L., Cai, P.L., Dong, J., Wang, J.S., Li, R.K., & Song, X.F. (2021). Assessment of the dynamic exposure to PM<sub>2.5</sub>  
748 based on hourly cell phone location and land use regression model in Beijing. *International Journal of*  
749 *Environmental Research and Public Health*, 18, <https://doi.org/10.3390/ijerph18115884>.
- 750 Liu, T.T., Gong, S.L., He, J.J., Yu, M., Wang, Q.F., Li, H.R., Liu, W., Zhang, J., Li, L., Wang, X.G., Li, S.L., Lu, Y.L., Du,  
751 H.T., Wang, Y.Q., Zhou, C.H., Liu, H.L., & Zhao, Q.C. (2017). Attributions of meteorological and emission factors  
752 to the 2015 winter severe haze pollution episodes in China's Jing-Jin-Ji area. *Atmospheric Chemistry and Physics*,  
753 17, 2971-2980, <https://doi.org/10.5194/acp-17-2971-2017>.
- 754 Liu, Z., Xiang, Y., Pan, Y., Zhang, T., Xu, W., & Li, L. (2024). Unveiling 3-D evolution and mechanisms of ozone pollution  
755 in Changzhou, China: Insights from lidar observations and modelling. *Environmental Pollution*, 359, 124556,  
756 <https://doi.org/10.1016/j.envpol.2024.124556>.
- 757 Liu, Z.R., Hu, B., Wang, L.L., Wu, F.K., Gao, W.K., & Wang, Y.S. (2015). Seasonal and diurnal variation in particulate  
758 matter (PM<sub>10</sub> and PM<sub>2.5</sub>) at an urban site of Beijing: analyses from a 9-year study. *Environmental Science and*  
759 *Pollution Research*, 22, 627-642, <https://doi.org/10.1007/s11356-014-3347-0>.
- 760 Ma, P., Zhang, Z., Zhang, Y., Lamu, Y., & Za, D. (2023). Effect of meteorological conditions on PM<sub>10</sub> concentrations in  
761 the middle reaches of the Yarlung Zangbo River, Tibet Plateau. *Theoretical and Applied Climatology*, 151, 725-737,  
762 <https://doi.org/10.1007/s00704-022-04330-y>.
- 763 Mehta, M., Khushboo, R., Raj, R., & Singh, N. (2021). Spaceborne observations of aerosol vertical distribution over Indian  
764 mainland (2009-2018). *Atmospheric Environment*, 244, <https://doi.org/10.1016/j.atmosenv.2020.117902>.
- 765 Miao, Y.C., Guo, J.P., Liu, S.H., Zhao, C., Li, X.L., Zhang, G., Wei, W., & Ma, Y.J. (2018). Impacts of synoptic condition



- 766 and planetary boundary layer structure on the trans-boundary aerosol transport from Beijing-Tianjin-Hebei region  
767 to northeast China. *Atmospheric Environment*, 181, 1-11, <https://doi.org/10.1016/j.atmosenv.2018.03.005>.
- 768 Mishra, A.K., & Shibata, T. (2012). Climatological aspects of seasonal variation of aerosol vertical distribution over central  
769 Indo-Gangetic belt (IGB) inferred by the space-borne lidar CALIOP. *Atmospheric Environment*, 46, 365-375,  
770 <https://doi.org/10.1016/j.atmosenv.2011.09.052>.
- 771 Ou, J., Hu, Q., Liu, H., Hong, Q., Xing, C., Tan, W., Lin, H., Wang, X., Xu, H., Zhu, P., & Liu, W. (2021). Vertical  
772 characterization and potential sources of aerosols in different seasons over the Yangtze River Delta using ground-  
773 based MAX-DOAS. *Environmental Pollution*, 279, <https://doi.org/10.1016/j.envpol.2021.116898>.
- 774 Qian, Z., Li, L., Lin, X., Sun, R., & Chen, Y. (2024). Spatial and temporal variation of PM<sub>2.5</sub> and the influence of vegetation  
775 in the Yangtze River Delta region. *Atmospheric Pollution Research*, 15, <https://doi.org/10.1016/j.apr.2024.102266>.
- 776 Shen, L., Cheng, Y., Bai, X., Dai, H., Wei, X., Sun, L., Yang, Y., Zhang, J., Feng, Y., Li, Y.J., Chen, D.-R., Liu, J., & Gui,  
777 H. (2022). Vertical profile of aerosol number size distribution during a haze pollution episode in Hefei, China.  
778 *Science of the Total Environment*, 814, <https://doi.org/10.1016/j.scitotenv.2021.152693>.
- 779 Shi, C.N., Yuan, R.M., Wu, B.W., Meng, Y.J., Zhang, H., Zhang, H.Q., & Gong, Z.Q. (2018). Meteorological conditions  
780 conducive to PM<sub>2.5</sub> pollution in winter 2016/2017 in the Western Yangtze River Delta, China. *Science of the Total*  
781 *Environment*, 642, 1221-1232, <https://doi.org/10.1016/j.scitotenv.2018.06.137>.
- 782 Shim, K., Kim, M.-H., Lee, H.-J., Nishizawa, T., Shimizu, A., Kobayashi, H., Kim, C.-H., & Kim, S.-W. (2022).  
783 Exacerbation of PM<sub>2.5</sub> concentration due to unpredictable weak Asian dust storm: A case study of an extraordinarily  
784 long-lasting spring haze episode in Seoul, Korea. *Atmospheric Environment*, 287,  
785 <https://doi.org/10.1016/j.atmosenv.2022.119261>.
- 786 Siddique, M.A., Naseer, E., Usama, M., & Basit, A. (2024). Estimation of surface-level NO<sub>2</sub> using satellite remote sensing  
787 and machine learning: A review. *Ieee Geoscience and Remote Sensing Magazine*, 12, 8-34,  
788 <https://doi.org/10.1109/mgrs.2024.3398434>.
- 789 Sun, W.B., Liu, Z.Y., Videen, G., Fu, Q., Muinonen, K., Winker, D.M., Lukashin, C., Jin, Z.H., Lin, B., & Huang, J.P.  
790 (2013). For the depolarization of linearly polarized light by smoke particles. *Journal of Quantitative Spectroscopy*  
791 *& Radiative Transfer*, 122, 233-237, <https://doi.org/10.1016/j.jqsrt.2012.03.031>.
- 792 Sun, X., Zhao, T., Hu, J., Bai, Y., Meng, L., Yang, Q., Zhou, Y., & Fu, W. (2024a). Inverse effects of aerosol radiative  
793 forcing on heavy PM<sub>2.5</sub> pollution of local accumulation and regional transport over central China. *Science of the*  
794 *Total Environment*, 917, <https://doi.org/10.1016/j.scitotenv.2024.170319>.
- 795 Sun, X., Zhou, Y., Zhao, T., Fu, W., Wang, Z., Shi, C., Zhang, H., Zhang, Y., Yang, Q., & Shu, Z. (2024b). Vertical



- 796 distribution of aerosols and association with atmospheric boundary layer structures during regional aerosol transport  
797 over central China. *Environmental Pollution*, 362, <https://doi.org/10.1016/j.envpol.2024.124967>.
- 798 Tombrou, M., Dandou, A., Helmis, C., Akylas, E., Angelopoulos, G., Flocas, H., Assimakopoulos, V., & Soulakellis, N.  
799 (2007). Model evaluation of the atmospheric boundary layer and mixed-layer evolution. *Boundary-Layer*  
800 *Meteorology*, 124, 61-79, <https://doi.org/10.1007/s10546-006-9146-5>.
- 801 Vakkari, V., Baars, H., Bohlmann, S., Bühl, J., Komppula, M., Mamouri, R.-E., & O'Connor, E.J. (2021). Aerosol particle  
802 depolarization ratio at 1565 nm measured with a Halo Doppler lidar. *Atmospheric Chemistry and Physics*, 21, 5807-  
803 5820, <https://doi.org/10.5194/acp-21-5807-2021>.
- 804 Wang, H., Sun, Z., Li, H., Gao, Y., Wu, J., & Cheng, T. (2018). Vertical-distribution characteristics of atmospheric aerosols  
805 under different thermodynamic conditions in Beijing. *Aerosol and Air Quality Research*, 18, 2775-2787,  
806 <https://doi.org/10.4209/aaqr.2018.03.0078>.
- 807 Wang, J., Wang, H., Zhang, C., Wang, Y., Zhang, Y., Zhou, J., Xu, W., Whalley, L.K., Dyson, J.E., Slater, E.J., Xing, C.,  
808 Chi, S., Wang, Y., Wang, L., Yu, X., Zeng, L., Lin, W., Zhao, W., Heard, D.E., Song, S., & Ye, C. (2025). Ozone  
809 production underestimation over the Tibetan Plateau: The role of NO<sub>x</sub> and OVOCs modeling uncertainties. *Journal*  
810 *of Geophysical Research-Atmospheres*, 130, <https://doi.org/10.1029/2025jd043321>.
- 811 Wang, J.L., Zhang, Y.H., Shao, M., Liu, X.L., Zeng, L.M., Cheng, C.L., & Xu, X.F. (2004). Chemical composition and  
812 quantitative relationship, between meteorological condition and fine particles in Beijing. *Journal of Environmental*  
813 *Sciences*, 16, 860-864
- 814 Wang, L.Y., Lyu, B.L., & Bai, Y.Q. (2020a). Aerosol vertical profile variations with seasons, air mass movements and local  
815 PM<sub>2.5</sub> levels in three large China cities. *Atmospheric Environment*, 224,  
816 <https://doi.org/10.1016/j.atmosenv.2020.117329>.
- 817 Wang, M., & Wang, H. (2021). Spatial distribution patterns and influencing factors of PM<sub>2.5</sub> pollution in the Yangtze River  
818 Delta: Empirical analysis based on a GWR model. *Asia-Pacific Journal of Atmospheric Sciences*, 57, 63-75,  
819 <https://doi.org/10.1007/s13143-019-00153-6>.
- 820 Wang, M., Wei, T., Lolli, S., Wu, K., Wang, Y., Hu, H., Yuan, J., Tang, D., & Xia, H. (2024). A long-term Doppler wind  
821 lidar study of heavy pollution episodes in western Yangtze River Delta region, China. *Atmospheric Research*, 310,  
822 <https://doi.org/10.1016/j.atmosres.2024.107616>.
- 823 Wang, Z., Liu, C., Hu, Q.H., Dong, Y.S., Liu, H.R., Xing, C.Z., & Tan, W. (2021). Quantify the Contribution of Dust and  
824 Anthropogenic Sources to Aerosols in North China by Lidar and Validated with CALIPSO. *Remote Sensing*, 13,  
825 <https://doi.org/10.3390/rs13091811>.



- 826 Wang, Z., Liu, C., Xie, Z.Q., Hu, Q.H., Andreae, M.O., Dong, Y.S., Zhao, C., Liu, T., Zhu, Y.Z., Liu, H.R., Xing, C.Z., Tan,  
827 W., Ji, X.G., Lin, J.N., & Liu, J.G. (2020b). Elevated dust layers inhibit dissipation of heavy anthropogenic surface  
828 air pollution. *Atmospheric Chemistry and Physics*, 20, 14917-14932, <https://doi.org/10.5194/acp-20-14917-2020>.
- 829 Xiang, Y., Zhang, T., Liu, J., Wan, X., Loewen, M., Chen, X., Kang, S., Fu, Y., Lv, L., Liu, W., & Cong, Z. (2021). Vertical  
830 profile of aerosols in the Himalayas revealed by lidar: New insights into their seasonal/diurnal patterns, sources,  
831 and transport\*. *Environmental Pollution*, 285, <https://doi.org/10.1016/j.envpol.2021.117686>.
- 832 Xiong, K., Xie, X., Mao, J., Wang, K., Huang, L., Li, J., & Hu, J. (2023). Improving the accuracy of O<sub>3</sub> prediction from a  
833 chemical transport model with a random forest model in the River Delta China. *Environmental Pollution*, 319,  
834 <https://doi.org/10.1016/j.envpol.2022.120926>.
- 835 Yang, S.M., Ma, Y.J., Zhang, W.Y., Lin, Z., Lu, Z.G., Zhou, X.J., Ren, Y.Z., Ren, X.B., Peng, K.C., Tan, Y.L., Wei, Y.M.,  
836 Ahmad, M., Zhao, D.D., Kong, L.B., Ma, Y.N., Tian, Y.L., & Xin, J.Y. (2025). The interaction of atmospheric  
837 boundary layer and PM pollution in Mongolian Plateau: Implication for the threshold control strategy. *Atmospheric  
838 Research*, 316, <https://doi.org/10.1016/j.atmosres.2025.107937>.
- 839 Yang, Y.J., Yim, S.H.L., Haywood, J., Osborne, M., Chan, J.C.S., Zeng, Z.L., & Cheng, J.C.H. (2019). Characteristics of  
840 heavy particulate matter pollution events over Hong Kong and their relationships with vertical wind profiles using  
841 high-time-resolution Doppler lidar measurements. *Journal of Geophysical Research-Atmospheres*, 124, 9609-9623,  
842 <https://doi.org/10.1029/2019jd031140>.
- 843 Yang, Z., Wang, Y., Xu, X.-H., Yang, J., & Ou, C.-Q. (2022). Quantifying and characterizing the impacts of PM<sub>2.5</sub> and  
844 humidity on atmospheric visibility in 182 Chinese cities: A nationwide time-series study. *Journal of Cleaner  
845 Production*, 368, <https://doi.org/10.1016/j.jclepro.2022.133182>.
- 846 Yu, H.J., Wang, Y.J., Peng, Q., Shao, Y.Q., Duan, C.M., Zhu, Y.F., Dong, S.R., Li, C.L., Shi, Y., Zhang, N., Zheng, Y.Y.,  
847 Chen, Y., Jiang, Q.W., Zhong, P.S., & Zhou, Y.B. (2020). Influence of coarse particulate matter on chickenpox in  
848 Jiading District, Shanghai, 2009-2018: A distributed lag non-linear time series analysis. *Environmental Research*,  
849 190, <https://doi.org/10.1016/j.envres.2020.110039>.
- 850 Yu, S., Liu, D., Xu, J., Wang, Z., Wu, D., Shan, Y., Shao, J., Mao, M., Qian, L., Wang, B., Xie, C., & Wang, Y. (2021).  
851 Optical properties and seasonal distribution of aerosol layers observed by lidar over Jinhua, southeast China.  
852 *Atmospheric Environment*, 257, <https://doi.org/10.1016/j.atmosenv.2021.118456>.
- 853 Zhan, Y., Xie, M., Zhuang, B., Gao, D., Zhu, K., Lu, H., Wang, T., Li, S., Li, M., Luo, Y., & Zhao, R. (2024). Particle-  
854 ozone complex pollution under diverse synoptic weather patterns in the Yangtze River Delta region: Synergistic  
855 relationships and the effects of meteorology and chemical compositions. *Science of the Total Environment*, 946,



- 856 174365, <https://doi.org/10.1016/j.scitotenv.2024.174365>.
- 857 Zhang, T., Che, H.Z., Gong, Z.Q., Wang, Y.Q., Wang, J.Z., Yang, Y.Q., Gui, K., & Guo, B. (2020a). The two-way feedback  
858 effect between aerosol pollution and planetary boundary layer structure on the explosive rise of PM<sub>2.5</sub> after the "Ten  
859 Statements of Atmosphere" in Beijing. *Science of the Total Environment*, 709,  
860 <https://doi.org/10.1016/j.scitotenv.2019.136259>.
- 861 Zhang, Y., Guo, J., Yang, Y., Wang, Y., & Yim, S.H.L. (2020b). Vertical wind shear modulates particulate matter pollutions:  
862 A perspective from radar wind profiler observations in Beijing, China. *Remote Sensing*, 12,  
863 <https://doi.org/10.3390/rs12030546>.
- 864 Zhong, J., Zhang, X., Dong, Y., Wang, Y., Liu, C., Wang, J., Zhang, Y., & Che, H. (2018). Feedback effects of boundary-  
865 layer meteorological factors on cumulative explosive growth of PM<sub>2.5</sub> during winter heavy pollution episodes in  
866 Beijing from 2013 to 2016. *Atmospheric Chemistry and Physics*, 18, 247-258, [https://doi.org/10.5194/acp-18-247-](https://doi.org/10.5194/acp-18-247-2018)  
867 [2018](https://doi.org/10.5194/acp-18-247-2018).  
868